Hybrid Position–Compliance Control for Selective Stiffening and Softening in Soft Continuum Robots

Danni Zhou and Jialei Shi

***Abstract*—Due to inherent compliance and flexibility, soft robots are well suited for tasks in unstructured environments that require safe interaction. However, this compliance also limits robot's payload capacity, highlighting the need for effective on-demand compliance regulation. This paper develops and validates a real-time position-compliance control approach (exceeding 2 kHz) for pneumatic soft continuum robots, enabling both position–compliance stiffening and softening based on a quasi-static Cosserat rod model. The proposed approach is experimentally validated in three scenarios: (i) position and compliance-stiffening control for path following under external disturbances, (ii) position and compliance-softening control for obstacle avoidance, and (iii) significance of selective compliance regulation. Overall, the proposed method enables selective softening for safe interaction and stiffening for path following under external loads, without relying on additional variable-stiffness mechanisms. Results highlight the importance of on-demand stiffening and softening control for enhancing robot–environment interaction capabilities.**

***Index Terms*—Pneumatic actuators, Soft continuum robots, Compliance stiffening and softening.**

I. Introduction

SOFT continuum robots are constructed from compliant materials such as silicones. Compared with rigid-body robots, soft robots are safer and more adaptable when interacting with objects in unstructured environments due to their compliant properties. However, this high compliance often results in limited payload capacity and increased control complexity. Therefore, it is crucial to modulate stiffness on demand and achieve effective compliance regulation [1], i.e., maintaining lower compliance during task execution while adopting higher compliance when navigating contact-rich environments.

A. Related Work

Current research on compliance control in soft robots can be broadly categorized into two main approaches: embedding variable-stiffness mechanisms and implementing model-based compliance control [2]. Variable-stiffness mechanisms enable compliance modulation by physically altering structural or material properties. Common strategies include rigidity-tunable materials [3], jamming structures [4], and antagonistic actuation. Jamming mechanisms employ granular or laminar materials whose stiffness increases when vacuumed. Antagonistic mechanism employs two or more actuators exerting opposing moments and thereby varies stiffness [5]. For example, [6] developed an antagonistic actuator comprising two symmetric pneumatic chambers. Simultaneous pressurization produced opposing bending moments and increased stiffness.

This work is supported by the Engineering and Physical Sciences Research Council, Grant EP/X033546/1 (*Corresponding author: Jialei Shi*).

Danni Zhou and Jialei Shi are with the Hamlyn Centre for Robotic Surgery, Department of Mechanical Engineering, Imperial College London, London, UK. (e-mail: j.shi@imperial.ac.uk).

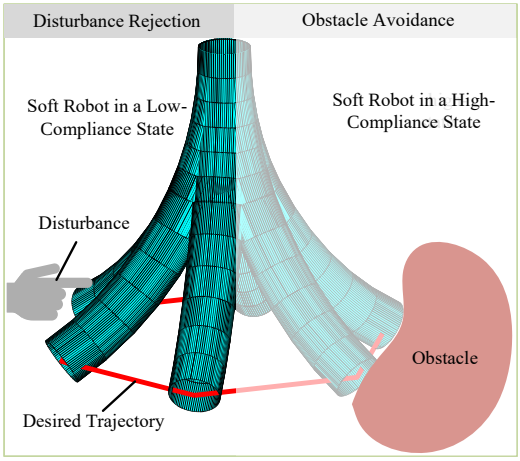

Fig. 1. Illustration of compliance control during path following: Maintaining low compliance enhances disturbance rejection (left), whereas higher compliance facilitates obstacle avoidance (right).

While effective, the above variable-stiffness mechanisms often rely on complex structures and specialized materials. Their size and integration requirements can hinder deployment in space-constrained scenarios (e.g., minimally invasive surgery). More importantly, these mechanisms typically produce global stiffness changes rather than modulating on-demand stiffness in task space. In contrast, many practical tasks, such as navigating confined anatomies and manipulating delicate tissues, benefit from directionally selective Cartesian stiffness control, enabling high compliance where safe interaction is needed while preserving rigidity along critical directions [7].

Model-based compliance control (e.g., impedance control) provides an alternative approach for compliance regulation in soft robots [8]. Existing studies have primarily focused on pneumatically driven variable-stiffness joints [9]. Representative examples include backstepping-based stiffness and position control for a two-degree-of-freedom soft robotic joint [10], force-feedback-based position and stiffness regulation of pneumatic robotic joints [11], adaptive control strategies for pneumatic rotary joints [12], and softening control of pneumatic muscle-actuated manipulators to enhance interaction safety [13]. However, compared with pneumatically driven joints, soft continuum robots present significantly greater challenges due to their high deformation, distributed compliance, and effectively infinite degrees of freedom [14]. For instance, [15] developed a stiffness controller for a concen-

tric tube robot without embedding additional stiffening mechanisms. Using a kinematics model, the controller computed a virtual force from the measured and reference tip positions and an adjustable stiffness matrix. [16] introduced a stiffness controller for a dual-segment tendon-driven soft robot using RGB-D vision to detect end-effector deviations caused by axial loads. More recently, [7] presented an algorithm that regulates both the posture and segment stiffness to control Cartesian stiffness. However, these compliance regulation approaches of soft continuum robots focus on stiffening control (increase stiffness), while active softening control remains less explored.

In summary, model-based compliance control reduces reliance on physical stiffening mechanisms, lowering weight and complexity while improving adaptability. Nevertheless, there remains a need for on-demand compliance regulation in soft continuum robots that enables both stiffening and softening for different tasks, particularly when embedding variable-stiffness mechanisms is challenging.

B. Contributions and Outline

This work proposes a real-time hybrid position-compliance control approach for hyper-plastic soft continuum robots exhibiting non-linear material properties. In particular, this work enables soft robots to maintain lower compliance when following desired trajectories, while exhibiting higher compliance when navigating in contact with environments.

The main contribution of this work lies in the development and validation of a hybrid position–compliance control strategy for soft continuum robots that enables selective stiffening and softening in task space without relying on any additional variable-stiffness mechanisms. In addition, this work experimentally highlights the importance of hybrid position–compliance stiffening and softening in Cartesian space during soft robot–environment interaction.

The rest of this paper is structured as follows: Section II details the position-compliance control strategy. The experimental setup and parameter identification are reported in Section III. Section IV presents the experimental validation, and Section V discusses findings from the validation results. Section VI concludes this work and identifies future research.

II. Methodology of the Hybrid Position-Compliance Stiffening/Softening Control

A. Soft Robot Prototype

The soft robot is a large-scale manipulator originally developed in [17] for steering a soft-everting robot. Its enlarged dimensions in this work are intended to increase payload capacity and facilitate compliance measurement. The robot is pneumatically actuated and consists of fully reinforced silicone chambers arranged symmetrically around a central lumen. The robot has an overall length of 115 mm and an external radius of 11.5 mm. The central lumen, with a radius of 5 mm, provides space for instrumentation and surgical tools. Nine chambers are designed to generate sufficient bending moments while maximising the central working channel. In particular, three adjacent chambers are internally connected into three pairs arranged at a 120° interval, enabling omni-directional bending motions. The actuation pressure vector is defined as $P = (P_1, P_2, P_3)$. Each chamber has an internal radius of 2.25 mm and is positioned 8.25 mm from the central axis. To constrain excessive longitudinal elongation, a nylon fabric is integrated into the central lumen.

B. Hybrid Position-Compliance Stiffening/Softening Control

1) Spring-based tip compliance regulation: The control objective is to actively modulate the robot's interaction behaviour between assistive (softening) and resistive (stiffening) modes while controlling tip trajectory, which falls within the impedance control paradigm [18]. In this work, the interaction compliance control has two assumptions: i) the environment is significantly stiffer than robots, ii) the system operates under quasi-static conditions, and dynamic effects are negligible. Specifically, impedance control specifies a desired dynamic relationship between position and force, typically represented by a virtual mass–spring–damper model. When dynamic terms are neglected, the general form of impedance control reduces to compliance control [8], yielding

$$F_v = k_f(p_m - p_r) = c_f^{-1}(p_m - p_r), \tag{1}$$

where the interaction compliance is regulated by a virtual force $F_v \in \mathbb{R}^{3\times1}$, generated by multiplying position difference between measured position p_m and reference position p_r by a virtual 3×3 stiffness matrix $k_f = c_f^{-1}$, and c_f is its inverse, a 3×3 compliance matrix. Specifically, positive values of k_f generate restoring forces that oppose external disturbances, resulting in increased effective stiffness (i.e., resistive behaviour), whereas negative values correspond to reduced stiffness, producing assistive forces aligned with the disturbance. It is important to emphasise that negative k_f does not represent a physical negative stiffness, but rather a control-induced interaction behaviour within a force-based impedance control framework. To ensure control stability, the magnitude of k_f is bounded such that stable interaction can be maintained [8].

Considering the robot subjected to F_v in a configuration g_c, linearizing the equilibrium equations at the robot's tip yields the local compliance matrix $C^b \in \mathbb{R}^{6\times6}$, relating a small applied wrench $W^b \in \mathbb{R}^6$ to an incremental twist $\delta\xi^b \in \mathbb{R}^6$:

$$\delta\xi^b = C^b\, W^b, W^b = [R^T f_v;\ 0_{3\times1}], \tag{2}$$

where $\xi^b, C^b,$ and W^b are written in the body frame, and R is the rotation matrix of the robot's tip. The new deformed configuration g_d can be calculated via

$$g_d = g_c e^{(\xi^b)^\wedge} = g_c e^{(C^b \mathbf{W}^b)^\wedge}, \tag{3}$$

where $(\cdot)^\wedge$ maps a twist from $\mathbb{R}^6$ to $\mathbb{R}^{4\times4}$ [14]. The tip displacement Δp is obtained as the difference between the translational components of the homogeneous transformations g_d and g_c, i.e., by subtracting their fourth columns. After computing Δp, the control objective is to compensate this deformation so the manipulator realizes the desired endpoint stiffness. The new

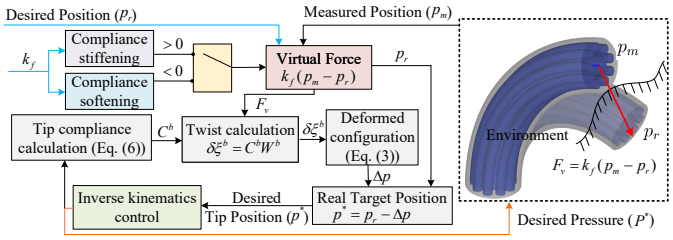

Fig. 2. Architecture of the proposed hybrid position-compliance stiffening and softening control method, where blue and orange arrows denote inputs and outputs, respectively.

target tip position p^* is updated by subtracting the predicted deformation Δp from the reference position p_r:

$$p^* = p_r - \Delta p. \tag{4}$$

This position compensation enables regulation of the robot's compliance behavior under unknown external loading.

To achieve p^*, the inverse kinematics solver computes the optimal chamber pressures P^* [19]:

$$P^* = \arg\min_{P} \left\| p(P) - p^* \right\|^2, \tag{5}$$

where $p(P)$ is a tip position vector computed from the robot forward kinematics. The computed P^* is sent to pressure regulators. The new endpoint p_m is measured, and the procedure repeats in the next cycle. To obtain the tip compliance matrix C^b in (2), the theoretical compliance distribution $C(s)^b$ along the robot is computed with the robot kinematics, as reported in the following section.

2) Cartesian tip compliance calculation: The Cartesian compliance along the robot backbone is computed the position vector $p(s)$ and the rotation matrix $R(s)$. $s \in [0, L]$ is the curve length along robot's backbone. The derivation of the compliance modeling approach is reported in [14]; readers are referred to this work for further details. Specifically, the global compliance matrix $C(s)^o$ is obtained via

$$\begin{cases} p_s(s) = R(s)v(s), \\ R_s(s) = R(s)\hat{u}(s), \\ n_s(s) = -f_e(s) + f_P(s), \\ m_s(s) = -\hat{p}_s(s)n(s) - l_e(s) + l_P(s), \\ C(s)_s^o = \mathrm{Ad}_{ob}^{-T}(s)c^b\mathrm{Ad}_{ob}^{-1}(s), \end{cases} \tag{6}$$

$\hat{(\cdot)}$ denotes the standard hat map from $\mathbb{R}^3$ to $\mathfrak{so}(3)$, such that for any $a, b \in \mathbb{R}^3$, $\hat{a}\, b = a \times b$. $p_s(s)$, $R_s(s)$, $n_s(s)$, and $m_s(s)$ are the derivatives of the position vector $p(s)$, the rotation matrix $R(s)$, the internal force $n(s)$, and the internal moment $m(s)$, respectively. $v(s)$ and $u(s)$ are the local strain and the curvature vectors. $f_e(s)$ and $l_e(s)$ are the distributed external force and moment. $f_P(s)$ and $l_P(s)$ are the distributed force and moment from pressure. $c^b = \mathrm{diag}[c^b_{se}, c^b_{bt}]$, is compliance density matrix in the body frame. $c^b_{se} = \mathrm{diag}[GA, GA, EA]^{-1}$, $c^b_{bt} = \mathrm{diag}[EI_x, EI_y, GJ_z]^{-1}$. G and E and are the shear and Young's moduli. I_x, I_y and J_z are the second moment of area around the x, y and z- axes. Ad_{ob} is the adjoint matrix. Please refer to [14] for details of (6). Finally, the compliance matrix C^b in the body frame is converted from $C^o(s)$ by

$$C^b = \mathrm{Ad}_{ob}(s)|_{s=L}^T C^o(s)|_{s=L}\mathrm{Ad}_{ob}(s)|_{s=L}. \tag{7}$$

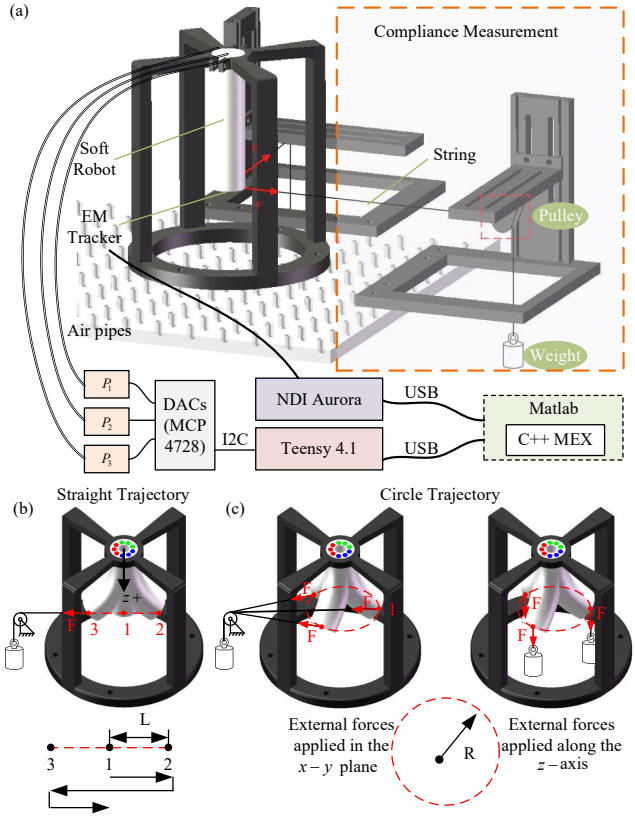

Fig. 3. (a) Illustration of the experimental setup. During kinematic characterization, the string is disconnected. For position–compliance control experiments, the robot tracks prescribed trajectories under external tip loads, such as (b) straight-line (a half length of L) and (c) circular paths (a radius of R).

In summary, the hybrid position-compliance stiffening and softening control strategy is illustrated in Fig. 2. Specifically, compliance stiffening or softening is achieved by assigning different values to k_f to compute the virtual restoring force f_v, thereby adjusting the robot's compliance behavior. By combining f_v with the modeled compliance matrix C^b in (6), the resulting deformed tip displacement Δp is obtained. The displacement Δp is then used to compute a new target position p^*, which serves as the input to the inverse kinematics to derive the desired actuation pressure.

III. Implementation and Parameter Identification

A. Experimental Setup

As illustrated in Fig. 3, the soft robot is mounted on a rigid 3D-printed structure bolted to a plastic baseboard. For compliance characterization, a loading apparatus (highlighted in orange) is positioned adjacent to the robot. This apparatus consists of a two-axis translation frame with adjustable arms, enabling calibrated loads to be applied at the robot tip along arbitrary planar directions. The frame can be repositioned along the x- and y-axes, allowing controlled loading in each direction. Calibrated weights (10–50 g) are applied via a string routed through a low-friction pulley mounted on the loading arm, thereby generating a consistent tip force along the prescribed direction. The robot tip position is measured using an electromagnetic (EM) tracker (Aurora, NDI).

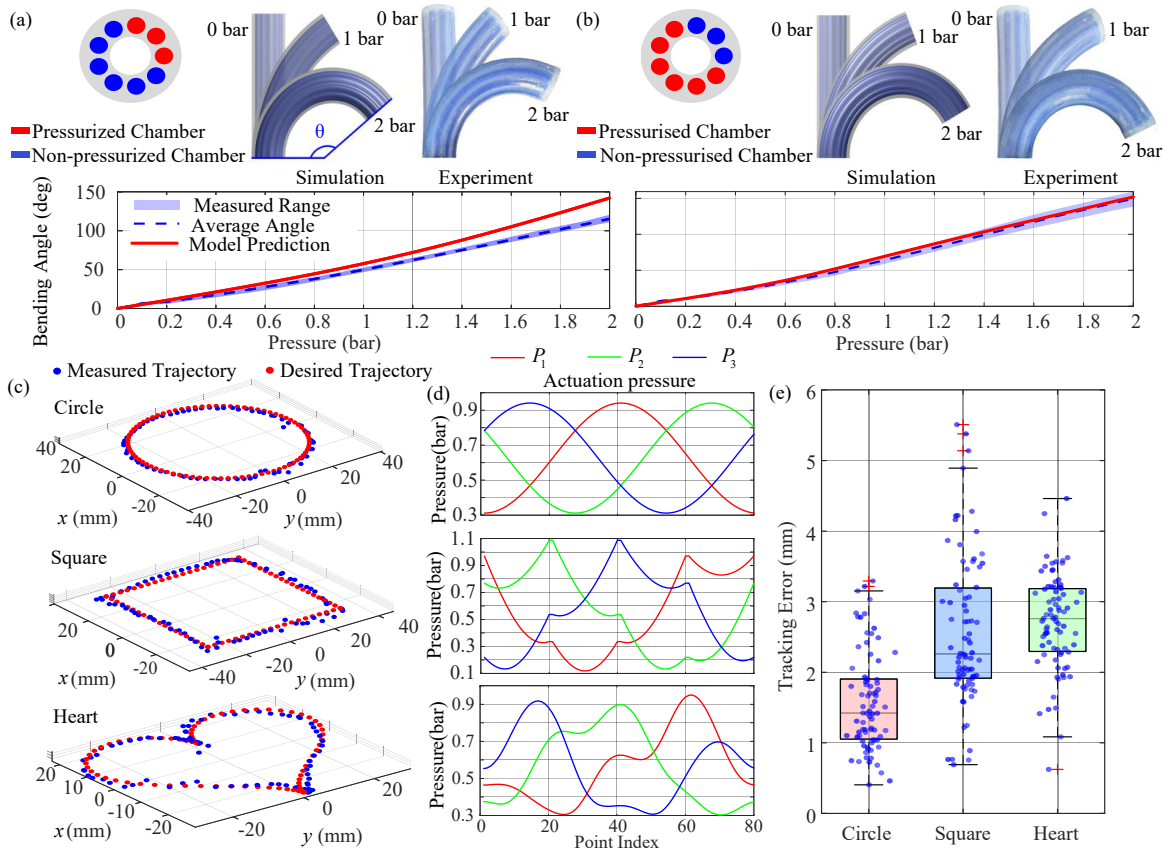

Fig. 4. Results for forward and inverse kinematics based on identified parameters: Bending angles subject to actuation of (a) one and (b) two chamber sets. The boundaries of the shaded regions indicate the maximum and minimum measured values. (c) Inverse kinematics control for three trajectories in one trial, with (d) corresponding actuation pressure in one trial and (e) corresponding errors in all trials.

The actuation pressures in the three chamber sets are regulated using three pressure regulators (SMC ITV2010). A microcontroller (Teensy 4.1) interfaces with two digital-to-analog converters (Adafruit MCP4728) via the I^{2}C protocol to generate the pressure control signals ($0 \sim 5$ V). The compliance control algorithm is implemented as a C++ MEX function and executed within MATLAB. MATLAB communicates with both the Teensy board, Adafruit boards, and the Aurora EM tracking system via serial interfaces. In experiments, the sampling frequency of the EM tracker was 20 Hz, and microcontroller operates at 100 Hz to control pressure.

B. Implementation and Parameter Identification

To identify the pressure-dependent effective modulus $E(P)$ of the soft manipulator, both forward and inverse kinematics tests were conducted. In forward kinematics test, applied actuation pressured increased and corresponding bending angles θ_m was measured using the EM tracker at each pressure step. The effective Young's modulus $E(P)$ was identified by minimizing the difference between the predicted bending angle $\theta_{\text{model}}(E, P)$ from the Cosserat rod model and the measured angle θ_m:

$$E(P) = \arg\min_{E} \left(\theta_{\text{model}}(E, P) - \theta_m\right)^2. \tag{8}$$

This procedure was repeated for all three single-pair (P_1, P_2, P_3) and three two-pair actuation configurations $(P_1\&P_2, P_2\&P_3, P_1\&P_3)$, and the resulting $E_{\text{single}}(P)$ and $E_{\text{two}}(P)$ curves were averaged to obtain the mean modulus curve $\bar{E}(P)$ for subsequent model fitting. The actuation pressure increased from 0 to 2 bar in 0.1 bar increments. Furthermore, $\bar{E}(P)$ obtained from (8) was fitted and refined by minimizing errors in the inverse kinematics control. Specifically, three trajectories are explored, including a reference circular trajectory with a radius of 30 mm, a square trajectory with a half-side length of 30 mm (60 mm full side), and a heart-shaped trajectory with a maximum width of 60 mm and height of 55 mm. All trajectories composed 80 points. Eventually, the optimized modulus $E^*(P)$ is

$$E^*(P) = 216.83 + 44.13 \tanh\big(1.414 - 1.113\, P_{sum}\big), \tag{9}$$

where P_{sum} is the summed pressure in bar and equals $P_1 + P_2 + P_3$, and $E^*(P)$ has a unit in kPa.

Results of the forward and inverse kinematics are reported in Figs. 4(a)-(b) and Figs. 4(c)-(e), respectively. The mean bending angle errors under single- and two-chamber actuation are 12.61° and 3.38°, respectively. Figs. 4(c) and 4(e) report that

TABLE I
COMPARISON OF INVERSE KINEMATICS IMPLEMENTATIONS ACROSS MATLAB AND C++ MEX

	MATLAB	C++ Mex in MATLAB
Integration Scheme	RK4	RK4
Solver	`fsolve` (LM)	Custom LM solver
Execution Speed	40 ms	0.4 ms

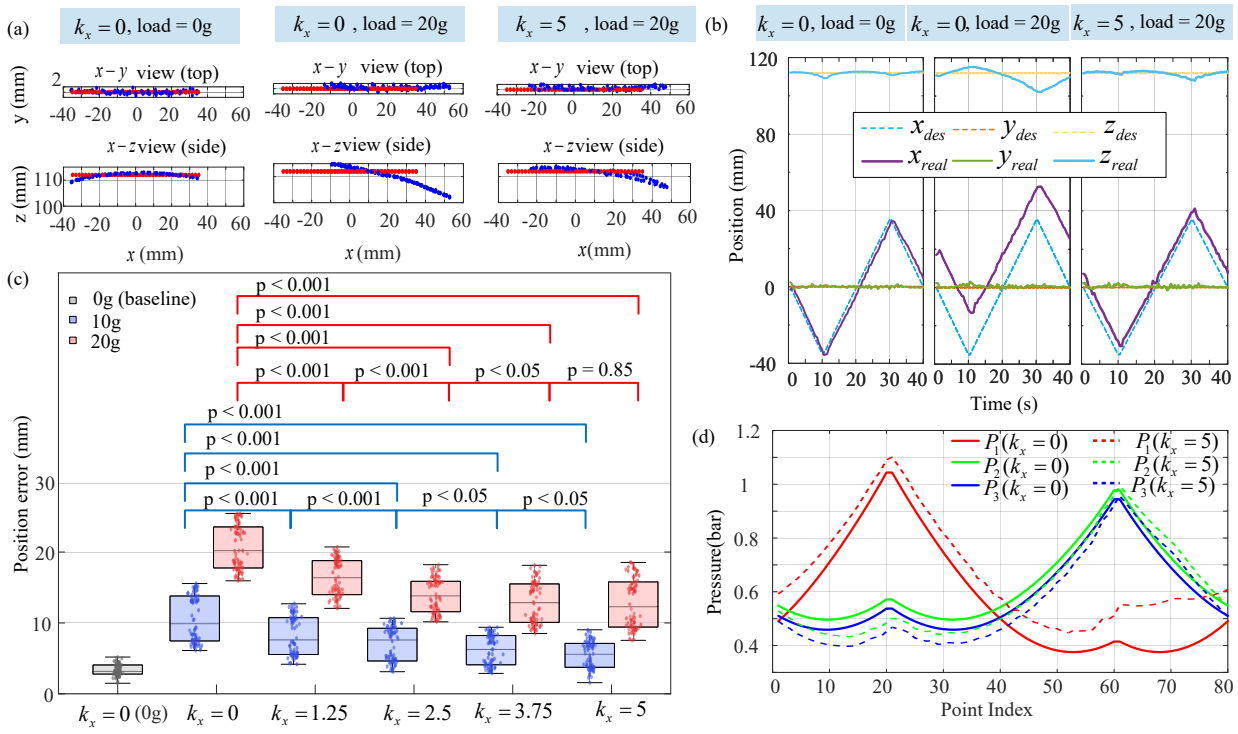

Fig. 5. Results for Experiment 1: (a) Straight-line path following in one trial under different stiffness gains $k_x = 0,\ 5$ mN/mm with a 20 g external load, shown in top, and side views. (b) Corresponding positions versus time. (c) Summarized tracking error in all trials under different stiffness gains $k_x = 0,\ 1.25,\ 2.5,\ 3.75,\ 5$ mN/mm with external loads of 0 g (baseline), 10 g, and 20 g. The sample size is 240 in each Welch's t-test.(d) Actuation pressure in one trial (P_1, P_2, P_3) when $k_x = 0, 5$ mN/mm with a 20 g external load.

for the circular trajectory, the RMSE is 3.09 mm using $E^*(P)$. Similarly, the RMSE is 3.02 mm for the square trajectory and 2.84 mm for the heart-shaped trajectory, respectively. Fig. 4(d) reports the actuation pressure patterns for three trajectories.

Table I compares the computation speed of the inverse solver across MATLAB and C++ MEX. All simulations were conducted on an HP Z2 Tower G9 Workstation equipped with an Intel Core i7-13700K CPU (3.4 GHz) and 64 GB RAM. MATLAB requires approximately 40 ms per computation. In contrast, The MEX interface integrates the C++ core, achieving 0.4 ms per computation while preserving MATLAB's data acquisition, making it well-suited for rapid integration and experimental validation. Above results confirm the real-time computation speed (>2 kHz) and the identified modulus $E^*(P)$ achieves reliable model prediction and path following accuracy. As such, $E^*(P)$ is adopted in following position-compliance control experiments in Section IV.

IV. Experimental Validation of the Hybrid Position-Compliance Control

Building on the experimental setup described in Section III-A and identified parameters in Section III-B, this section reports experimental validation of the hybrid position-compliance control, including (i) position and compliance-stiffening control for path following, (ii) position and compliance-softening control for obstacle avoidance, and (iii) significance of selective compliance control. Pairwise two-sided Welch's two-sample t-tests were performed in MATLAB using `ttest2()` with a (95%) confidence interval to compare position tracking errors under different stiffness gains. Since each trial was independently initialized, the measurements were treated as independent samples. The null hypothesis assumed equal mean tracking errors between groups, while the alternative hypothesis assumed unequal means.

A. Experiment 1- Position and Compliance-Stiffening Control for Path Following

1) Experimental Protocol: The robot followed different paths under external loads with compliance-stiffening control. Two trajectories were prescribed: a straight line along the x-axis with a half-length $L = 35$ mm and a circular path in the x–y plane with a radius $R = 25$ mm (see Figs. 3(b)-(c)). External loads were applied using calibrated weights of 10 g and 20 g. Three loading conditions were investigated: (i). In-line disturbance along $+x$ axis during the straight path following (see Fig. 3(b)), with $k_x \in \{0,\ 1.25,\ 2.5,\ 3.75,\ 5\}$ mN/mm and $k_y = k_z = 0$ mN/mm. (ii). In-plane disturbance during the circular path following with varying force directions (see Fig. 3(c)). Stiffness parameters were set as $k_x = k_y \in \{0,\ 1.25,\ 2.5,\ 3.75,\ 5\}$ mN/mm and $k_z = 0$ mN/mm. (iii). Vertical disturbance applied along the $+z$ when following the same circular trajectory (see Fig. 3(c)), with $k_z \in \{0,\ 10,\ 20\}$ mN/mm and $k_x = k_y = 0$ mN/mm. In each case, the robot was initialized at the trajectory start point; the load was then applied; and the trajectory was executed with the prescribed stiffness gain factors (k_x, k_y, k_z). Tip position and chamber pressures were recorded. Each trial repeated three times.

2) Results: (i). Straight-line path following with in-line loads: Fig. 5(a) shows the measured trajectories under a 20 g external loading when stiffness gains $k_x = 0,$ and 5 mN/mm.

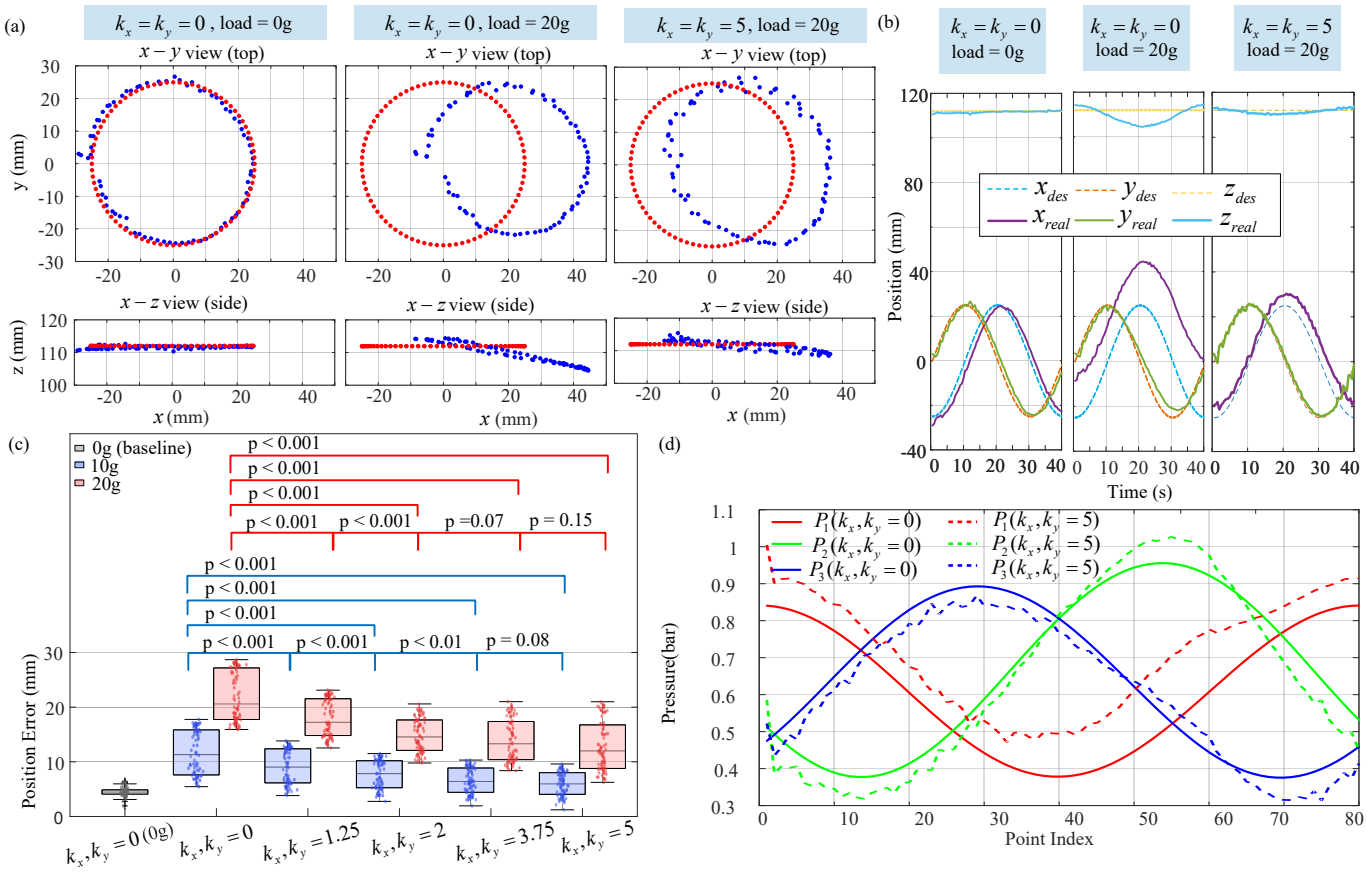

Fig. 6. Results for Experiment 1: Circular path following in one trial under two stiffness gains $k_x = k_y = 0,\ 5$ mN/mm with 0 and 20 g external loads, shown in top, and side views. (b) Corresponding positions versus time. (c) Summarized tracking error in all trials under different stiffness gains $k_x = k_y = 0,\ 1.25,\ 2.5,\ 3.75,\ 5$ mN/mm with external loads of 0 g (baseline), 10 g, and 20 g. The sample size is 240 in each Welch's t-test. (d) Actuation pressure (P_1, P_2, P_3) in one trial when $k_x = k_y = 0,\ 5$ mN/mm with a 20 g external load.

Without external loading ($k_x = 0$ mN/mm, load $= 0$ g), the robot accurately follows the desired path. As shown in Fig. 5(b), When a 20 g load is applied along the $+x$-axis without stiffness regulation ($k_x = 0$ mN/mm), the robot tip exhibits a drift of approximately 20 mm in the x-axis. In contrast, the drift is less than 8 mm when stiffness regulation is enabled ($k_x = 5$ mN/mm).

Fig. 5(c) summarizes trajectory errors with different loads and stiffness gain parameters. Under the 10 g load, the RMSE decreases from 10.8 mm at $k_x = 0$ mN/mm to 5.9 mm at $k_x = 5$ mN/mm, corresponding to a 45 % reduction. Under the 20 g load, the RMSE decreases from 20.7 mm at $k_x = 0$ mN/mm to 13.0 mm at $k_x = 5$ mN/mm, representing a 37 % reduction. Under the 10 g load, most pairwise comparisons yield highly significant differences ($p < 0.001$), indicating that increasing k_x effectively reduced the trajectory error. Similarly, under the 20 g load, the difference between $k_x = 0$ and $k_x = 5$ mN/mm is highly significant ($p < 0.001$), while the error from $k_x = 3.75$ mN/mm to $k_x = 5$ mN/mm is not statistically significant ($p = 0.85$).

Fig. 5(d) compares the pressure profiles (P_1, P_2, P_3) under a 20 g external load for $k_x = 0,\ 5$ mN/mm. With $k_x = 5$ mN/mm, P_1 increases while P_2 and P_3 reduce. At the first endpoint (index ≈ 20), P_1 increases from 1.04 bar to 1.09 bar, while P_2 and P_3 decrease from 0.57 bar and 0.54 bar to 0.48 bar and 0.45 bar, respectively. At the second endpoint (index ≈ 60), P_1 rises from 0.41 bar to 0.51 bar, whereas P_2 and P_3 reduce slightly from 0.98 bar and 0.94 bar to 0.96 bar and 0.92 bar. Overall, stiffness regulation introduces an additional offset of up to about 0.10 bar for P_1 and about 0.09 bar reduction for P_2 and P_3.

(ii). Circular path following with x-y plane loads: Fig. 6(a) shows the measured circular trajectories for different stiffness gain factors under a 20 g in–plane loads. Compared with the desired path, applying an in-plane disturbance causes a maximum drift of 20 mm along the x-axis. When the commanded stiffness gain is set to $k_x = 5\,\mathrm{mN/mm}$, the maximum drift is less than 10 mm (see Fig. 6(b)). Fig. 6(c) summarizes all tracking errors. Under the 10 g load, the RMSE decreases from 11.93 mm at $k = 0$ mN/mm to 6.69 mm at $k = 5$ mN/mm, corresponding to a 44 % reduction. Similarly, under the 20 g load, the RMSE decreases from 22.27 mm at $k = 0$ mN/mm to a minimum of 14.33 mm at $k = 3.75$ mN/mm (36 % reduction), before slightly increasing to 15.32 mm at $k = 5$ mN/mm. Additionally, for the 10 g load, most pairwise comparisons yield highly significant differences ($p < 0.001$), confirming that increasing k substantially improves trajectory accuracy. For the 20 g load, the difference between $k = 0$ and $k = 3.75$ mN/mm was highly significant ($p < 0.001$), while the improvement from $k = 3.75$ mN/mm to $k = 5$

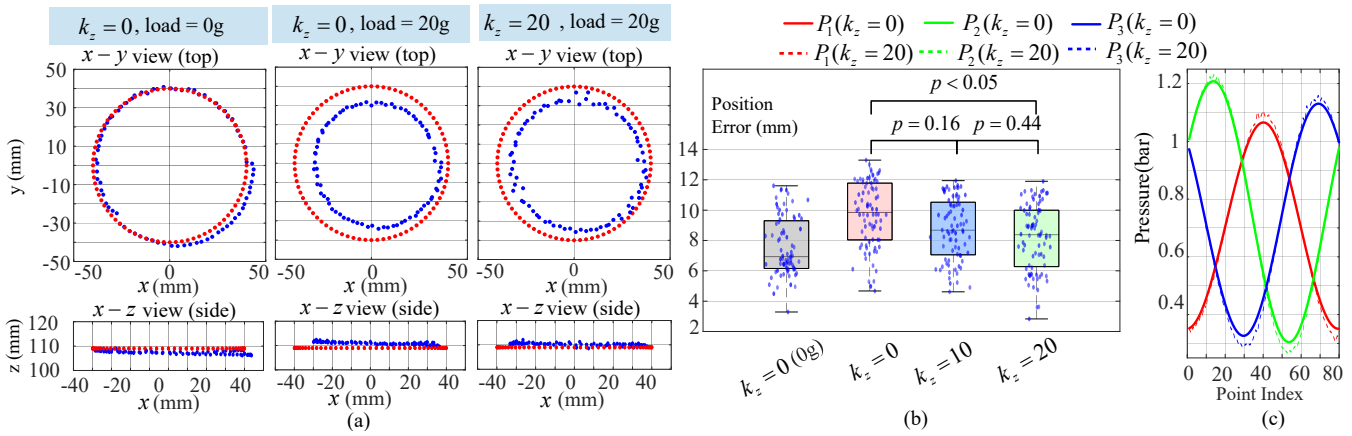

Fig. 7. Results for Experiment 1: (a) Circular path following in one trial under different vertical stiffness gains $k_z = 0,\ 20$ mN/mm with a 20 g vertical load, shown in top, and side views. (b) Summarized tracking errors under different vertical stiffness gains $k_z = 0,\ 10,\ 20$ mN/mm with a 20 g vertical load. The sample size is 240 in each Welch's t-test. (c) Actuation pressure in one trial with different vertical stiffness gains $k_z = 0,\ 20$ mN/mm under a 20 g vertical load.

mN/mm was not statistically significant ($p = 0.15$). These results demonstrate that larger stiffness gains effectively reduce trajectory error, but the benefit saturates beyond $k = 3.75$ mN/mm under higher loading conditions. Fig. 6(d) presents the actuation pressure profiles (P_1, P_2, P_3) under a 20 g in-plane load for $k_x = k_y = 0$ and 5 mN/mm. Without stiffness control, all three pressures exhibit approximately sinusoidal patterns during circular trajectory tracking. When stiffness regulation is enabled ($k_x = k_y = 5$ mN/mm), P_1 shifts upward, while P_2 and P_3 are also modulated with smaller amplitude variations. At the endpoint located along the positive x-axis (index ≈ 40), P_1 increases from 0.37 bar to 0.50 bar. Around pressure peaks and valleys, P_2 and P_3 exhibit smaller pressure variations of approximately 0.07 bar.

(iii). Circular path following with vertical loads: Fig. 7(a) reports circular trajectories under a vertical load of 20 g with two stiffness settings, i.e., $k_z \in \{0, 20\}$ mN/mm, compared against the unloaded case ($k_z = 0$ mN/mm, load = 0 g). When $k_z = 0$ mN/mm, the applied vertical load causes a downward shift of the entire trajectory in the z-direction and a radial contraction in the x–y plane. Increasing k_z effectively keeps measured trajectories closer to the desired circular path. The RMSE values over the full trajectory are summarized in Fig. 7(b). From $k_z = 0$ mN/mm to $k_z = 20$ mN/mm, the RMSE decreases from 9.19 mm to 7.30 mm, i.e., a 21 % reduction. At the intermediate setting of $k_z = 10$ mN/mm, the RMSE is 8.02 mm. Moreover, the error reduction in RMSE from $k_z = 0$ mN/mm to $k_z = 20$ mN/mm is statistically significant ($p < 0.05$), whereas the differences between $k_z = 0$ and $k_z = 10$ mN/mm ($p = 0.16$), as well as between $k_z = 10$ and $k_z = 20$ mN/mm ($p = 0.44$), are not significant.

Fig. 7(c) reports chamber pressures. Without regulation, the pressures have a sinusoidal pattern. With $k_z = 20$ mN/mm, the command pressure increases around the peaks and decreases around valleys, with a maximum change of 0.03 bar.

B. Experiment 2- Position and Compliance-Softening Control for Obstacle Avoidance

1) Experimental Protocol: The robot was tested for obstacle avoidance during path following by applying compliance-softening control. Four trajectories were commanded: two planar paths in the x–y plane (a circular trajectory with a radius of $R = 25$ mm and a square trajectory with a side length of $L = 50$ mm) and two spatial helical paths in 3D space (a cylindrical helix and a square helix) with a vertical increment of $\Delta z = 0.5$ mm per revolution and $N = 15$ turns. A cylindrical obstacle ($r = 20$ mm, $h = 35$ mm) was placed such that the desired paths intersected obstacle boundary. Two control strategies were compared: (i) *No compliance regulation*, where stiffness gains were set to $k_x = k_y = 0$ mN/mm along the entire trajectory; and (ii) *Region-based softening*, where negative stiffness gains ($k_x = k_y = -3$ mN/mm) were applied only within a predefined region around the obstacle to reduce stiffness along the x- and y-axes, while the robot executed without compliance regulation outside the contact region. During each run, the tip position was recorded using the EM tracker, and chamber pressures were saved.

2) Results: Fig. 8 presents the results of obstacle avoidance when tracking a 2D path. In Fig. 8(a), the obstacle is initially located at $(x = 40, y = 5)$ mm, intersecting the desired circular trajectory (red) with a maximum penetration depth of 4.7 mm. Without compliance regulation, the measured path (blue) follows the desired path. As a result, the robot's outer contour (green circles), reconstructed from the EM sensor, penetrates the obstacle region, indicating physical contact. Consequently, the obstacle is displaced from its initial position to $(x = 48, y = 1)$ mm, $(x = 50, y = 1)$ mm, and $(x = 50, y = 0)$ mm across repeated trials, where the obstacle displacement is 10.3 ± 1.2 mm. By contrast, in Fig. 8(b), negative gains ($k_x = k_y = -3$ mN/mm) are applied over trajectory points 35–65 (i.e., contact during $10.5 \sim 19.5$ seconds) to locally reduce robot stiffness, while the remainder of the trajectory is executed without regulation ($k_x = k_y = 0$ mN/mm). The robot trajectory adapts to the obstacle boundary without displacing the obstacle.

Figs. 8(c)–(d) report the square-trajectory case, where the obstacle is initially located at $(x = 40, y = -2)$ mm, with a maximum penetration depth of 5.0 mm into the desired path. Without compliance control ($k_x = k_y = 0$ mN/mm), the measured paths track the desired square, yet the robot

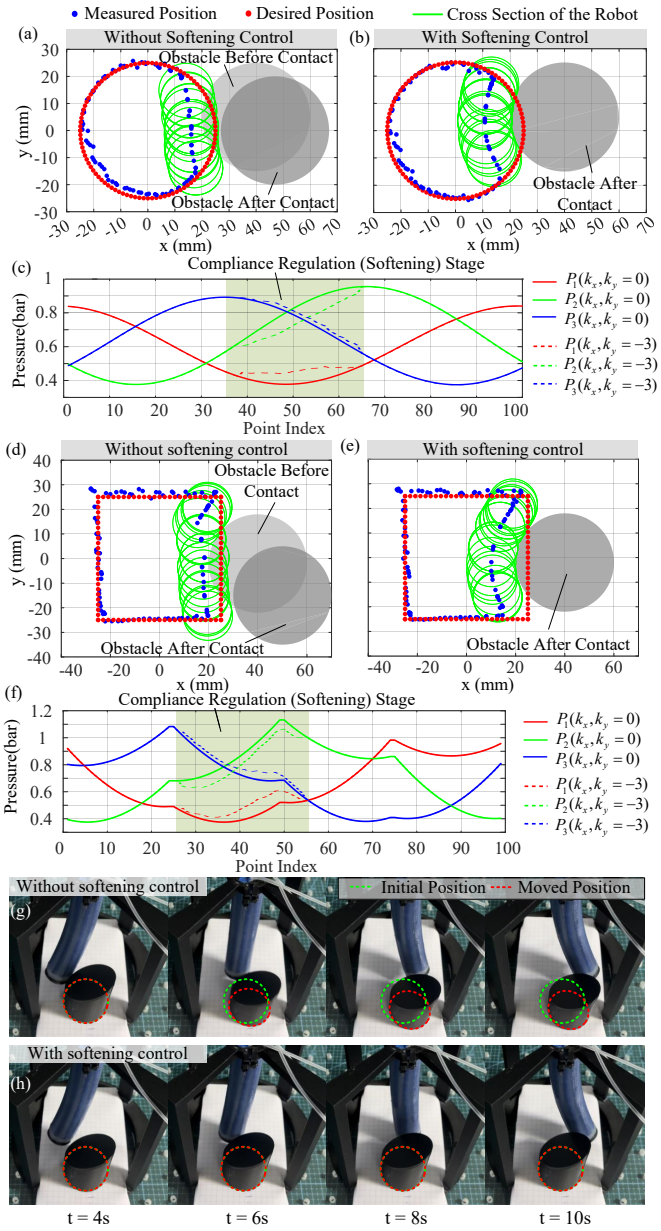

Fig. 8. Results for Experiment 2: 2D obstacle avoidance. Circular trajectory in one trial (a) without compliance regulation ($k_x = k_y = 0$ mN/mm) and with compliance regulation ($k_x = k_y = -3$ mN/mm). (c) Corresponding control pressures. (d) Square trajectory in one trial without compliance regulation ($k_x = k_y = 0$ mN/mm) and with compliance regulation ($k_x = k_y = -3$ mN/mm). (f) Corresponding control pressures. Snapshots of square path following in one trial: (g) without compliance regulation, the robot displaces the obstacle; (h) with region-based softening ($k_x = k_y = -3$ mN/mm, points 25–55), the robot slides over the obstacle while the obstacle remains at its initial position.

(green circle) intrudes into the obstacle region. The obstacle is consequently displaced to three nearby locations over repeated trials: $(x = 51, y = -17)$ mm, $(x = 51, y = -16)$ mm, and $(x = 52, y = -17)$ mm, where the obstacle displacement is 18.5 ± 0.7 mm. With region-based softening control ($k_x = k_y = -3$ mN/mm) applied only at trajectory points 25–55 and $k_x = k_y = 0$ mN/mm elsewhere, the path adapts to obstacle surface (i.e., contact during $5 \sim 11$ seconds); and the robot follows the desired path outside the softening region.

Figs. 8(c) and (f) show the actuation pressures for the circular and square trajectories, respectively. Without compliance regulation (solid lines), the pressures follow the nominal pattern required for trajectory tracking. Within the softening regions, P_1 (driving bending away from the obstacle) increases, while P_2 (facing the obstacle) decreases; P_3 exhibits a slight increase. Outside these regions, all pressures return to their nominal profiles. Figs. 8(g)–(h) present snapshots from the square-path experiment. Without compliance regulation, the robot displaces the obstacle upon contact. In contrast, with region-based softening (points 25–55), the robot tip follows the obstacle boundary, while the obstacle remains stationary. With softening control ($k_x = k_y = -3$ mN/mm), the robot trajectory consistently deforms to follow the obstacle boundary in both circular and rectangular paths, maintaining sliding contact without observable obstacle displacement, achieving a 100% obstacle-avoidance success rate.

Fig. 9 shows the obstacle avoidance when tracking 3D paths. In Fig. 9(a), the obstacle is intially located at $(x = 40, y = 5)$ mm with a maximum penetration depth of 4.7 mm. Without compliance regulation, the robot's outer cross-sectional envelope (green circles) penetrates the obstacle volume. The obstacle is pushed away to three locations over repeated runs: $(x = 49, y = 1)$ mm, $(x = 48, y = 0)$ mm, and $(x = 51, y = 0)$ mm. The displaced distance of the obstacle is 10.3 ± 1.6 mm. By contrast, in Fig. 9(b), a region-based softening is used where negative gains ($k_x = k_y = -3$ mN/mm) are applied only within a predefined region around the obstacle. In this mode, the measured path follows the obstacle boundary, and the contact time is 9 seconds per revolution.

Fig. 9(c) shows the corresponding actuation pressure (P_1, P_2, P_3) for the cylindrical spiral trajectory. In the baseline case ($k_x = k_y = 0$ mN/mm), the pressures follow the nominal periodic pattern required for spiral motions. When compliance regulation is activated within the highlighted softening region, the chamber pressures facing the obstacle (P_2) are dynamically reduced, while the opposite chamber (P_1) increases accordingly. This coordinated redistribution of chamber pressures reduces robot's stiffness, enabling obstacle avoidance.

Similarly, Figs. 9(d)-(f) present the results for the square helix trajectory. In Fig. 9(d), the obstacle is placed at $(x = 40, y = -2)$ mm, and the desired square spiral trajectory (red) intersects the obstacle region, with a maximum penetration depth of 5.0 mm into the desired path. Without compliance regulation, the measured trajectories closely follow the desired path, causing the robot's cross-sections to penetrate the obstacle volume, which leads to repeated collisions and displaces the obstacle to three nearby locations: $(x = 51, y = -18)$ mm, $(x = 50, y = -17)$ mm, and $(x = 53, y = -18)$ mm, where the obstacle displacement is 19.4 ± 1.3 mm. With compliance regulation, as shown in Fig. 9(e), the trajectory adapts to the obstacle shape in 3D space, with a contact time of 6 seconds per revolution (green area). After bypassing the obstacle, the trajectory returns to the desired square spiral trajectory.

Fig. 9(f) reports the corresponding actuation pressure (P_1, P_2, P_3) for the square spiral trajectory. Similarly to Fig. 9(c), the baseline pressures ($k_x = k_y = 0$ mN/mm) follow the periodic pattern, while compliance regulation results in

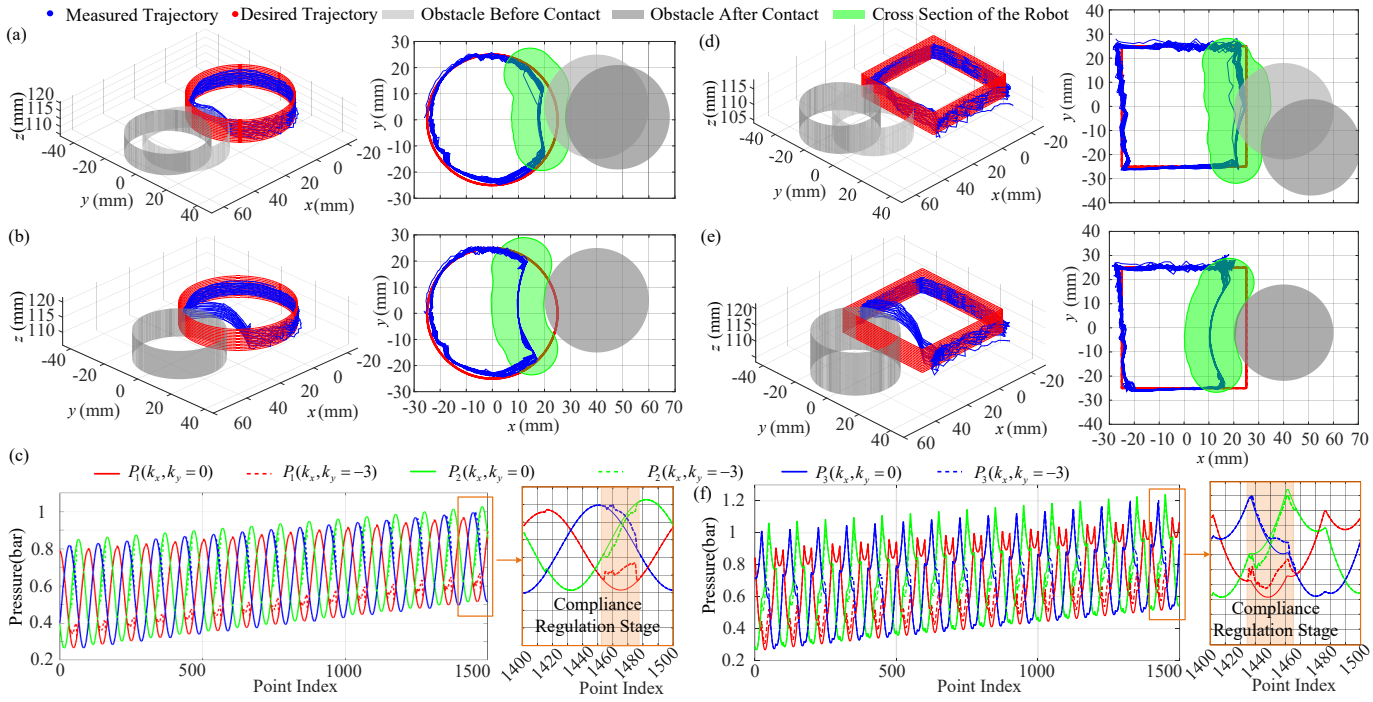

Fig. 9. Results for Experiment 2: 3D obstacle avoidance along the cylindrical helix trajectory in one trial, (a) without compliance regulation ($k_x = k_y = 0$ mN/mm) and (b) with compliance regulation ($k_x = k_y = -3$ mN/mm). The corresponding (c) actuation pressure profiles (P_1, P_2, P_3). 3D obstacle avoidance along the square helix trajectory, (d) without compliance regulation ($k_x = k_y = 0$ mN/mm), and (e) with compliance regulation ($k_x = k_y = -3$ mN/mm). (f) Actuation pressure profiles (P_1, P_2, P_3) in one trial.

reduced pressures in the chambers facing the obstacle and compensatory increases in the opposite chambers, reducing stiffness and enabling adaptive obstacle avoidance. With softening control, the soft robot avoids the obstacle in all trials.

C. Experiment 3-Significance of Selective Compliance Regulation

1) Experiment Protocol: The significance of selective compliance regulation was investigated. Similar to Experiment 2 (see Fig. 8), the robot was commanded to follow a circular trajectory with a radius of $R = 25$ mm. The same cylindrical obstacle ($r = 20$ mm, $h = 35$ mm) was placed such that the desired paths intersected with the obstacle. Two control strategies were compared: (i) *Full softening control*, where stiffness gains were set to $k_x = k_y = -3$ mN/mm along the entire trajectory; and (ii) *Region-based softening*, where negative stiffness gains ($k_x = k_y = -3$ mN/mm) were applied within a predefined region around the obstacle to reduce stiffness along the x- and y-axes, while the robot had no softening control out of the contact region.

2) Results: Fig. 10(a) shows that the robot avoids the obstacle with softening control, while the tracking errors from the full softening control mode are larger. Fig. 10(b) reports that the median tracking errors of region-based softening control and full softening control are 3.4 mm and 6.5 mm, respectively. Fig. 10(c) illustrates that the actuation pressure only varies during the contact area in the region-based softening mode. In contrast, three actuation pressures all have shifts during the whole test, and the pressure has the largest variation when the robot contacts with the obstacle.

V. Discussion of Validation Results

A. Discussion of Implementation and Parameter Identification

The identified $E^*(p)$ effectively captures the non-linear material behavior of the robot. From the bending experiments, it can be observed that the model slightly overestimates the bending angle under single-chamber set actuation, but matches the experimental results well under two-chamber set actuation (see Fig. 4(a)). This is because the selected $E^*(P)$ curve considers the inverse kinematics control, where most tasks involve multi-chamber actuation. While the modulus identification framework is transferable across different robots and experimental setups [20], accurate parameter identification remains necessary for each robotic system due to fabrication discrepancy and pressure control variations.

Errors are attributed to three factors: (i) residual offsets and drift in the NDI sensors can introduce measurement errors in tip position [14]; (ii) unmodeled viscoelasticity; and (iii) manufacturing tolerances, including minor variations in chamber radius, or wall thickness. Unmodeled viscoelasticity introduces rate-dependent tracking errors and may induce oscillations under rapid external loading, while manufacturing discrepancy leads to model mismatch. Future work will consider extending the current quasi-static model to incorporate viscoelastic dynamics, as well as automating fabrication processes to enhance consistency and reduce parameter uncertainty.

The overall computation speed in C++ is > 2 kHz (see Table I) and confirms the real-time capability of the proposed approach. This outperforms work in [21] where a speed of $30 \sim 50$ Hz is achieved. In addition, the gain parameters in this work were selected empirically to demonstrate the effectiveness of the proposed method, while also providing

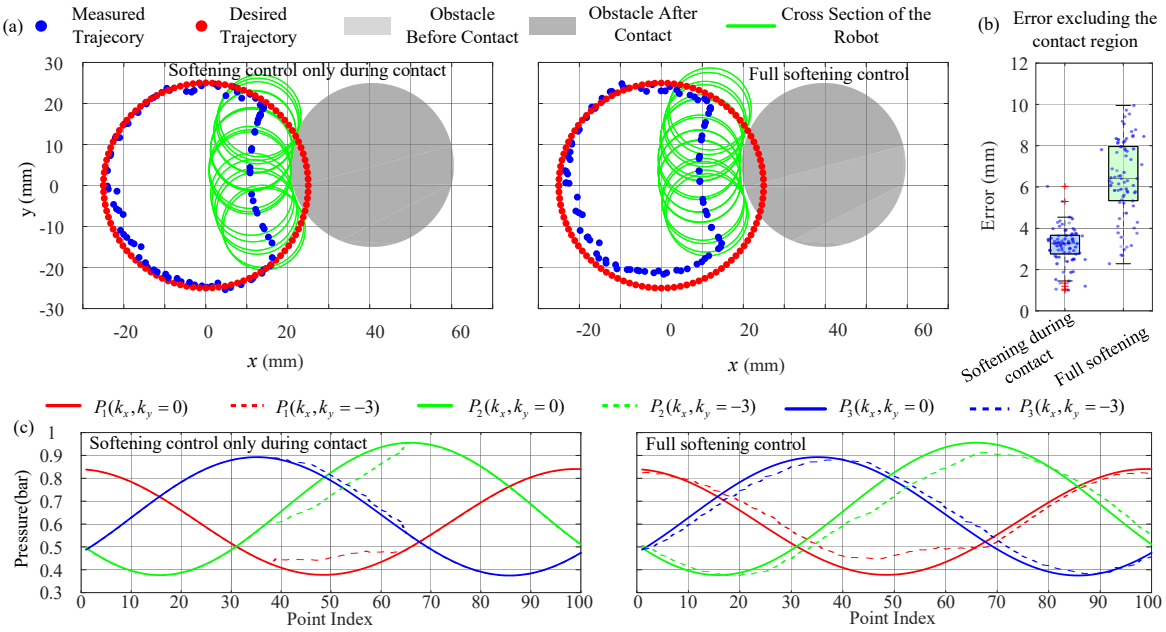

Fig. 10. Results for Experiment 3: Comparison between a selective softening control and fully softening control when following a circle. (a) Measured and desired trajectories in one trial. Summarised errors from all trials are in (b). (c) The actuation pressure patterns for selective softening control and full softening control in one trial.

useful initial guidelines for different applications. A systematic investigation of optimal parameter selection, such as model-based optimisation or learning-based tuning methods, remains an important direction for future work.

B. Discussion of Position-Compliance Regulation

The path following task under external loads in Experiment 1 illustrates a typical application of stiffness enhancement to mitigate disturbances [16]. It is worth noting that increasing tip loads reduces the robot's available range of motion, thereby constraining the set of feasible trajectories that can be accurately tracked. While the proposed stiffness stiffening ($< 100\%$) improves the robot's ability to resist tip loads and enhances tracking performance within this feasible workspace, it cannot fully compensate for the reduced range of motions, as shown in Figs. 6-7. In this work, compliance-stiffening is validated by applying external loads during trajectory tracking, demonstrating improved robustness to disturbances. Similar validation approaches have been reported in prior work, e.g., [16]. We acknowledge that motion planning becomes more complex in practical applications. Integrating compliance-stiffening with task-level planning in complex environments remains an important direction for future work.

As reported in Fig. 10 (Experiment 3), relative to full softening control, the region-based softening approach (negative gains limited to the contact region) yields smaller trajectory error outside contact. The reason is that tracking error is not zero, always-on softening continually converts that residual error in the inverse control, enlarging tracking errors. Restricting softening to the contact region removes this bias. These results highlight the significance of on-demand and selective compliance for safe, adaptive interaction in constrained environments. Potential applications include human–robot collaboration [18], peg-in-hole assembly in industrial automation, and navigation and manipulation in endoluminal robotic surgery [23].

As summarized in Table II, this work uniquely supports real-time, hybrid trajectory–compliance stiffening and softening control in Cartesian space, whereas existing studies primarily focus on stiffening control [7], [16], [22]. Although [21] investigates compliance softening control, its low computational speed limits real-time continuous trajectory–compliance control. In addition, the proposed method achieves directionally selective Cartesian compliance modulation and fundamentally differs from material rigidity–tuning approaches (e.g., LMPA [3]), which alter global structural stiffness rather than enabling on-demand, task-space compliance regulation.

It is noteworthy that this work focuses on low-motion tasks, such as laser ablation in robotic surgery, where soft robotic systems typically operate at low bandwidth (e.g., around 1 Hz [23]). Extending the quasi-static model to a dynamic Cosserat rod model and modelling actuation dynamics are a promising direction for future work, as it would enable the capture of dynamic effects such as actuator dynamics and inertial effects. Experimental evaluation of controller stability is provided in the Supplementary Document by sweeping the gain factors along the x-, y-, and z-axes. The results indicate that the proposed controller maintains stability for stiffness regulation within $\pm 100\%$ of the natural stiffness along the x- and y-axes. In contrast, when regulating stiffness along the z-axis, stability is preserved within a narrower regulation range of approximately -50% to $+100\%$. Similar behaviour was reported in [15] for a tendon-driven continuum robot, where stiffness along the x- and y-axes could be increased or decreased by approximately $\pm 100\%$; however, stiffness regulation along the z-axis was not investigated.

The selective control considered in this work focuses on hybrid compliance stiffening or softening relative to pure posi-

TABLE II
COMPARISON BETWEEN OUR COMPLIANCE CONTROL APPROACHES AND EXISTING WORKS FOR CONTINUUM ROBOTS

Reference	Actuation	Compliance-varying Principle	Variable-stiffness Structure	Trajectory-Compliance Control	Stiffening Range	Softening Range	Computation Speed	Control Bandwidth
[7]	Tendon	Pressure regulation	Yes	Yes	Up to $+300\%$	No	< 1 Hz	N/A
[15]	Concentric tube	Tube length	No	No	$\approx +100\%$	$\approx -50\%$	1 kHz	≈ 5 Hz
[16]	Tendon	Tendon tension	Yes	Yes	$\approx +100\%$	No	N/A	N/A
[22]	Pressure	Antagonistic pressure	No	Yes	$\approx +100\%$	No	N/A	N/A
[21]	Pressure	Pressure regulation	No	No	$\approx +100\%$	$\approx -25\%$	≈ 20 Hz	N/A
Our work	Pressure	Pressure regulation	No	Yes	$+70\% \sim +100\%$	$-60\% \sim -20\%$	> 2 kHz	< 5 Hz*

The stiffening/softening range is calculated as the increase/decrease in compliance/stiffness relative to natural values; < 5 Hz* is estimated from [20].

tion control, rather than the simultaneous combination of both modes. Assigning positive and negative gains concurrently may introduce additional complexity in the inverse kinematics, which could affect solvability under certain conditions. An investigation of such coupled effects requires further analysis and is beyond the scope of this work.

VI. CONCLUSION

This paper presented the development and validation of a real-time hybrid position–compliance control strategy that enables both stiffening and softening in soft continuum robots. Experimental results demonstrate that the proposed approach allows selective compliance softening for safe interaction or stiffening for disturbance rejection along desired directions. Notably, the method achieves this by exclusively regulating actuation pressure without relying on additional variable-stiffness mechanisms. Future work will incorporate contact sensing to switch between softening and stiffening modes, thereby assessing its practical performance in cluttered, uncertain environments and during on-demand manipulation tasks.

REFERENCES

[1] G. A. Naselli and B. Mazzolai, "The softness distribution index: towards the creation of guidelines for the modeling of soft-bodied robots," *Int. J. Rob. Res.*, vol. 40, no. 1, pp. 197–223, 2021.

[2] J. Shi, W. Gaozhang, S.-A. Abad, and H. Wurdemann, *Stiffness Modelling and Control for Soft Material Continuum Robotic Manipulators*. Cham: Springer Nature Switzerland, 2026, pp. 223–238.

[3] J. Peters *et al.*, "Actuation and stiffening in fluid-driven soft robots using low-melting-point material," in *Proc. IEEE/RSJ Int. Conf. Intell. Robots Syst.*, 2019, pp. 4692–4698.

[4] Y. Wei *et al.*, "A novel, variable stiffness robotic gripper based on integrated soft actuating and particle jamming," *Soft Rob.*, vol. 3, no. 3, pp. 134–143, 2016.

[5] K. Althoefer, "Antagonistic actuation and stiffness control in soft inflatable robots," *Nat. Rev. Mater.*, vol. 3, no. 6, pp. 76–77, 2018.

[6] S. M. Babu, A. Sadeghi, A. Mondini, and B. Mazzolai, "Antagonistic pneumatic actuators with variable stiffness for soft robotic applications," in *Proc. IEEE Int. Conf. Soft Robot.*, 2019, pp. 283–288.

[7] F. Stella, J. Hughes, D. Rus, and C. Della Santina, "Prescribing Cartesian stiffness of soft robots by co-optimization of shape and segment-level stiffness," *Soft Rob.*, vol. 10, no. 4, pp. 701–712, 2023.

[8] C. Ott, R. Mukherjee, and Y. Nakamura, "A hybrid system framework for unified impedance and admittance control," *J. Intell. Robot. Syst.*, vol. 78, no. 3, pp. 359–375, 2015.

[9] R. Richardson, M. Brown, B. Bhakta, and M. Levesley, "Impedance control for a pneumatic robot-based around pole-placement, joint space controllers," *Control Eng. Pract.*, vol. 13, no. 3, pp. 291–303, 2005.

[10] N. Herzig, R. Moreau, T. Redarce, F. Abry, and X. Brun, "Nonlinear position and stiffness backstepping controller for a two degrees of freedom pneumatic robot," *Control Eng. Pract.*, vol. 73, pp. 26–39, 2018.

[11] B. Ugurlu, P. Forni, C. Doppmann, E. Sariyildiz, and J. Morimoto, "Stable control of force, position, and stiffness for robot joints powered via pneumatic muscles," *IEEE Trans. Ind. Informat.*, vol. 15, no. 12, pp. 6270–6279, 2019.

[12] M. Trumić, K. Jovanović, and A. Fagiolini, "Decoupled nonlinear adaptive control of position and stiffness for pneumatic soft robots," *Int. J. Rob. Res.*, vol. 40, no. 1, pp. 277–295, 2021.

[13] T.-Y. Choi, B.-S. Choi, and K.-H. Seo, "Position and compliance control of a pneumatic muscle actuated manipulator for enhanced safety," *IEEE Trans. Control Syst. Technol.*, vol. 19, no. 4, pp. 832–842, 2011.

[14] J. Shi *et al.*, "Stiffness modelling and analysis of soft fluidic-driven robots using Lie theory," *Int. J. Rob. Res.*, vol. 43, no. 3, pp. 354–384, 2024.

[15] M. Mahvash and P. E. Dupont, "Stiffness control of surgical continuum manipulators," *IEEE Trans. Robot.*, vol. 27, no. 2, pp. 334–345, 2011.

[16] J. Lai, B. Lu, and H. K. Chu, "Variable-stiffness control of a dual-segment soft robot using depth vision," *IEEE/ASME Trans. Mechatronics*, vol. 27, no. 2, pp. 1034–1045, 2021.

[17] J. Shi, K. Borvorntanajanya, K. Chen, E. Franco, and F. R. y. Baena, "Design, control, and evaluation of a novel soft everting robot for colonoscopy," *IEEE Trans. Robot.*, vol. 41, pp. 4843–4859, 2025.

[18] X. Zhao, Y. Chen, L. Qian, B. Tao, and H. Ding, "Human–robot collaboration framework based on impedance control in robotic assembly," *Engineering*, vol. 30, pp. 83–92, 2023.

[19] J. Shi, S. Abad Guaman, J. Dai, and H. Wurdemann, "Position and orientation control for hyperelastic multisegment continuum robots," *IEEE/ASME Trans. Mechatronics*, vol. 29, no. 2, pp. 995–1006, 2024.

[20] J. Shi, S.-A. Abad, J. S. Dai, and H. Wurdemann, "Compliance model-based contact force control for soft continuum robots," *Soft Rob.*, vol. 13, no. 2, pp. 310–323, 2026.

[21] J. Shi *et al.*, "Model-based static compliance analysis and control for pneumatic-driven soft robots," *IEEE/ASME Trans. Mechatronics*, vol. 30, no. 6, pp. 5567–5578, 2025.

[22] D. Bruder, M. A. Graule, C. B. Teeple, and R. J. Wood, "Increasing the payload capacity of soft robot arms by localized stiffening," *Sci. Rob.*, vol. 8, no. 81, p. eadf9001, 2023.

[23] G. Fang *et al.*, "Soft robotic manipulator for intraoperative mri-guided transoral laser microsurgery," *Sci. Robot.*, vol. 6, no. 57, p. eabg5575, 2021.

Danni Zhou received the B.S. degree in Agriculture Engineering from the Zhejiang University, China, in 2024, and the M.S. degree in Advanced Mechanical Engineering from the Imperial College London, UK, in 2025. Her research interests include design and control of soft robotic manipulators.

Jialei Shi received the B.S. degree in Naval Architecture and Ocean Engineering from the Harbin Institute of Technology, China, in 2017, and the M.S. degree in Aerospace Engineering from the Beijing Institute of Technology, China, in 2019, and the Ph.D. degree in Mechatronic and Robotic Engineering from the University College London, UK, in 2024. He was a visiting student at Tsinghua University, from 2017-2019. He is currently a Research Associate in the Hamlyn Centre, Imperial College London. His research interests include design, modelling and control of soft robotics and medical devices. He is recognized as a 2024 RSS Pioneer.

Supplementary Material for Hybrid Position–Compliance Control for Selective Stiffening and Softening in Soft Continuum Robots

Danni Zhou and Jialei Shi

This document includes experiments which investigated stability and performance of the compliance controller with different gain parameters.

S.I. Analysis of Compliance Control Performance and Stability

A. Compliance Regulation under Various Gain Parameters

Stability and performances of compliance control were assessed by applying calibrated weights along the global x-, y-, and z-axes under different stiffness gains (see Fig. S1). Two robot configurations were assessed. For each robot configuration, stiffness was estimated from the load–displacement slope. During experiments, the positive gain factor was increased progressively until oscillations occurred, whereas the negative gain factor was increased until the robot was no longer able to return to its initial position after the removal of external loads.

1) Vertical (z-) direction loading: To characterise stiffness along the z-axis, the chamber pressures were adjusted to achieve four target stiffness gain factors $k \in \{-20,\ 0,\ 20,\ 40\}\,\mathrm{mN/mm}$. Calibrated weights of $25\,\mathrm{g}$ and $50\,\mathrm{g}$ were applied vertically to generate known external forces, as illustrated in Fig. S1(a). For each commanded stiffness setting and load level, the resulting vertical tip displacement Δd_z was recorded in real time using the Aurora electromagnetic tracking system, and the directional stiffness and compliance were calculated as:

$$K_z = \frac{F}{\Delta d_z} \tag{S1}$$

$$C_z = \frac{1}{K_z}, \tag{S2}$$

where F is the applied vertical force.

For z-direction tests, the two robot configurations were defined as:

- **Configuration 1:** $P_1 = 0.8\,\mathrm{bar},\ P_2 = P_3 = 0$ (bending along the $-x$ axis).
- **Configuration 2:** $P_1 = 1.0\,\mathrm{bar},\ P_2 = P_3 = 0$ (bending along the $-x$ axis).

2) Lateral (x-, y-) direction loading.: Similarly, the stiffness along the x- and y-axes was characterised by setting the commanded stiffness coefficient to $k \in \{-5,\ 0,\ 5,\ 10\}\,\mathrm{mN/mm}$ and applying calibrated weights of $10\,\mathrm{g}$, $20\,\mathrm{g}$, and $30\,\mathrm{g}$ along the positive x- or y-axis, as illustrated in Fig. S1(b). In each case, the applied load generated a known force F, and the corresponding tip displacements Δd_x and Δd_y were measured using the same tracking system to compute directional stiffness or compliance as:

$$K_x = \frac{F}{\Delta d_x}, \qquad K_y = \frac{F}{\Delta d_y}, \tag{S3}$$

$$C_x = \frac{1}{K_x}, \qquad C_y = \frac{1}{K_y}. \tag{S4}$$

For x/y-direction tests, the two robot configurations were chosen as:

- **Configuration 1:** $P_1 = 0.5\,\mathrm{bar},\ P_2 = P_3 = 0$ (bending along the $-x$ axis).
- **Configuration 2:** $P_2 = 0.5\,\mathrm{bar},\ P_1 = P_3 = 0$ (bending towards both the $-y$ and $+x$ axes).

All measurements were performed for both configurations and repeated three times. The average displacement across trials was used to calculate the reported stiffness values.

Danni Zhou and Jialei Shi are with the Hamlyn Centre for Robotic Surgery, Department of Mechanical Engineering, Imperial College London, London, UK. (e-mail: j.shi@imperial.ac.uk).

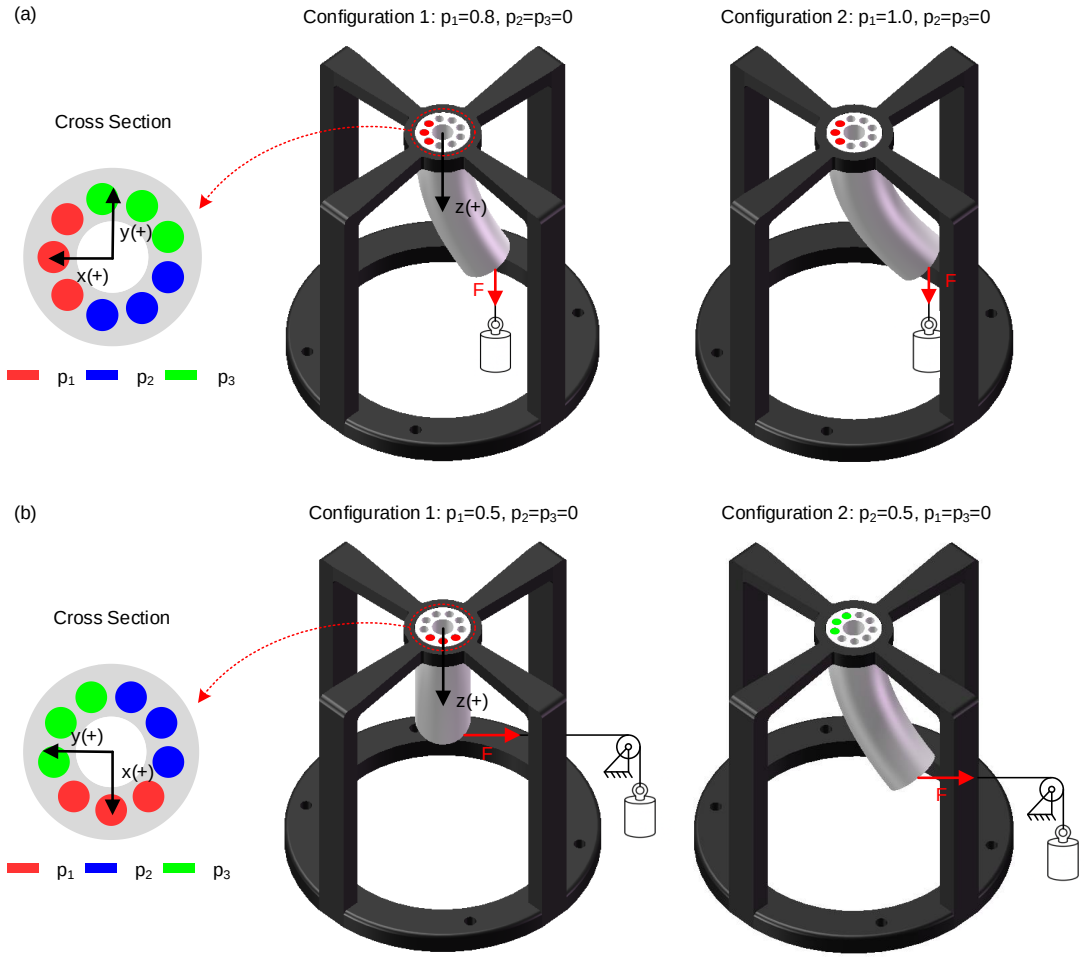

Fig. S1. Experimental setup for directional loading tests. (a) z-direction loading under two configurations ($P_1 = 0.8\,\mathrm{bar}$ and $P_1 = 1.0\,\mathrm{bar}$). (b) x- and y-direction loading under two configurations ($P_1 = 0.5\,\mathrm{bar}$ and $P_2 = 0.5\,\mathrm{bar}$).

B. Results

1) Results of vertical (z-) direction loading: Figs. S2(a) - (b) show the deflection–load relationships for Configurations 1 and 2, respectively. For Configuration 1, the natural compliance at $k_z = 0$ mN/mm was $0.10\,\mathrm{mm\,g^{-1}}$. When the gain was decreased to $k_z = -5$ mN/mm, the compliance increased to $0.13\,\mathrm{mm\,g^{-1}}$, representing a $30\,\%$ variation relative to the natural compliance. Conversely, increasing the gain to $k_z = 10$ mN/mm reduced the compliance to $0.06\,\mathrm{mm\,g^{-1}}$, corresponding to a $-40\,\%$ variation. For Configuration 2, the compliance was generally higher due to the larger bending angle, with a natural value of $0.16\,\mathrm{mm\,g^{-1}}$ at $k_z = 0$ mN/mm. At $k_z = -5$ mN/mm, the compliance further increased to $0.25\,\mathrm{mm\,g^{-1}}$, representing a $20.83\,\%$ variation. In contrast, increasing the gain to $k_z = 10$ mN/mm significantly reduced the compliance to $0.08\,\mathrm{mm\,g^{-1}}$, corresponding to a $-50\,\%$ variation.

Figs. S2(c) - (d) present the corresponding chamber pressure responses under a constant $50\,\mathrm{g}$ vertical load for four k_z settings. As observed from the figures, for both Configuration 1 and 2, only P_1 was actively modulated to regulate vertical stiffness, while P_2 and P_3 remained zero throughout the experiments. For the baseline case ($k_z = 0$ mN/mm), the steady-state pressure of P_1 was approximately $0.5\,\mathrm{bar}$. Increasing k_z above zero required raising P_1 to stiffen the robot, whereas negative gain settings reduced P_1 below $0.5\,\mathrm{bar}$, resulting in higher compliance. Fig. S2(e) further shows the transient tip displacement responses in Configuration 2, where the deflection rapidly stabilises within approximately $5\,\mathrm{s}$, demonstrating consistent steady-state compliance under different stiffness settings.

Table I summarizes the measured compliance and variation ratios relative to the natural values in both configurations. Positive variation ratios indicate an increase in compliance (softening), while negative ratios indicate a decrease (stiffening).

Overall, these results confirm that the stiffness gain k_z effectively modulates the vertical compliance of the robot, and the modulation effect becomes more pronounced with larger absolute gain values, as the change at $k_z = 40$ mN/mm is significantly greater than that at $k_z = 20$ mN/mm. Additionally, Configuration 2 consistently exhibits higher compliance than Configuration 1 across all stiffness settings, indicating that larger bending angles reduce the effective vertical stiffness of the soft continuum robot.

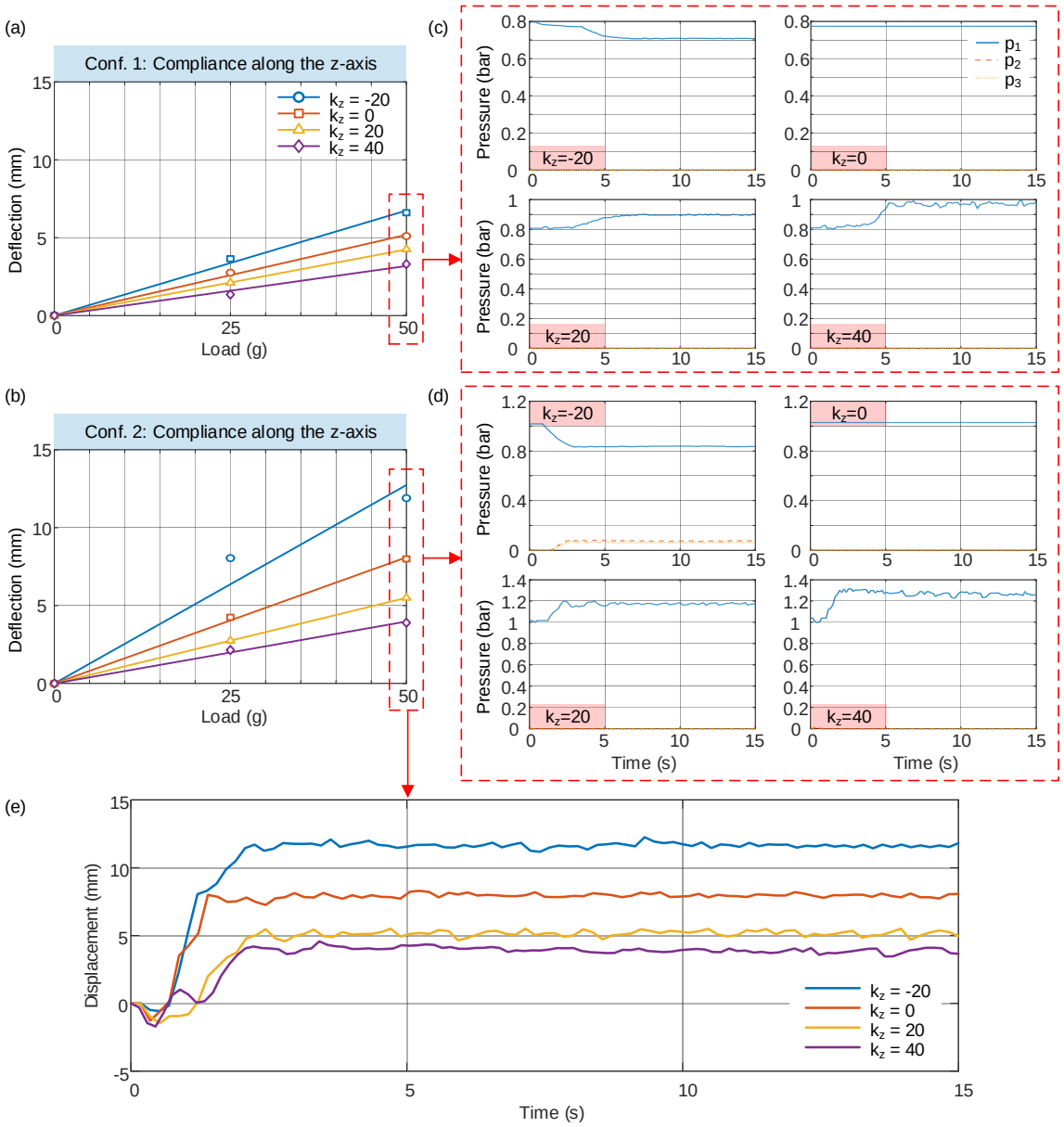

Fig. S2. Experimental results of directional stiffness validation under z- direction loading. (a) Deflection–load relationships for Configuration 1. (b) Deflection–load relationships for Configuration 2. (c) Pressure responses of P_1, P_2, and P_3 in Configuration 1 under a 50 g vertical load for four k_z settings ($k_z = -20$, 0, 20, 40 mN/mm). (d) Pressure responses of P_1, P_2, and P_3 in Configuration 2 under a 50 g vertical load for four k_z settings ($k_z = -20$, 0, 20, 40 mN/mm). (e) Time responses of end-tip displacement in Configuration 2 under a 50 g vertical load for four k_z settings.

2) Results of lateral (x-, y-) direction loading: Fig. S3(a) shows the deflection–load curves along the x- axis in Configuration 1. The natural compliance along the x- axis at $k_x = 0$ mN/mm was $0.62\,\mathrm{mm\,g^{-1}}$. Reducing the gain to $k_x = -5$ mN/mm increased compliance to $1.59\,\mathrm{mm\,g^{-1}}$ (156.45 %, softening), while increasing the gain to $k_x = 10$ mN/mm decreased it to $0.33\,\mathrm{mm\,g^{-1}}$ ($-46.77\,\%$, stiffening). Fig. S3(c) show the corresponding chamber pressures. When $k_x = 0$ mN/mm, $P_1 \approx 0.5\,\mathrm{bar}$ while $P_2 = P_3 \approx 0\,\mathrm{bar}$. When $k_x = -5$ mN/mm, P_1 decreases significantly, whereas P_2 and P_3 increase symmetrically. For $k_x = 5$ mN/mm and $k_x = 10$ mN/mm, P_1 increases to enhance stiffness, while P_2 and P_3 remain close to zero.

Fig. S3(b) show the deflection–load curves along the y-axis in Configuration 1. The natural compliance along the y- axis at $k_y = 0$ mm/mN was $0.70\,\mathrm{mm\,g^{-1}}$. At $k_y = -5$ mN/mm, the compliance increased to $1.55\,\mathrm{mm\,g^{-1}}$ (121.43 %, softening), while $k_y = 10$ mm/mN reduced it to $0.40\,\mathrm{mm\,g^{-1}}$ ($-42.86\,\%$, stiffening). Fig. 3(d) reports the chamber pressures. At $k_y = 0$ mN/mm, $P_2 \approx 0.5\,\mathrm{bar}$ and $P_1 = P_3 \approx 0\,\mathrm{bar}$. For $k_y = -5$ mN/mm, P_1 and P_2 both increase, the structure softens. For $k_y = 5$ mN/mm and $k_y = 10$ mN/mm, P_1 increases slightly, P_3 increases notably, while P_2 remain near zero, leading to stiffening effect.

TABLE SI
COMPLIANCE ALONG THE Z-AXIS UNDER DIFFERENT GAIN FACTORS (COLORS HIGHLIGHT VARIATION RATIOS: POSITIVE=RED, ZERO=GRAY, NEGATIVE=BLUE.)

		Configuration 1		Configuration 2	
	Gain factor	**Compliance[mm/g] (Stiffness[g/mm])**	**Variation ratio**	**Compliance[mm/g] (Stiffness[g/mm])**	**Variation ratio**
Compliance along the z-axis	$k_z = -20$	0.13 (7.69)	+30.00% (-23.10%)	0.25 (4)	+56.25% (-36.6%)
	$k_z = 0$	0.10 (10)	0%	0.16 (6.25)	0%
	$k_z = 20$	0.08 (12.5)	−20.00% (+25%)	0.11 (9.09)	−31.25% (+45.44%)
	$k_z = 40$	0.06 (16.67)	−40.00% (+66.67%)	0.08 (12.5)	−50.00% (+100%)

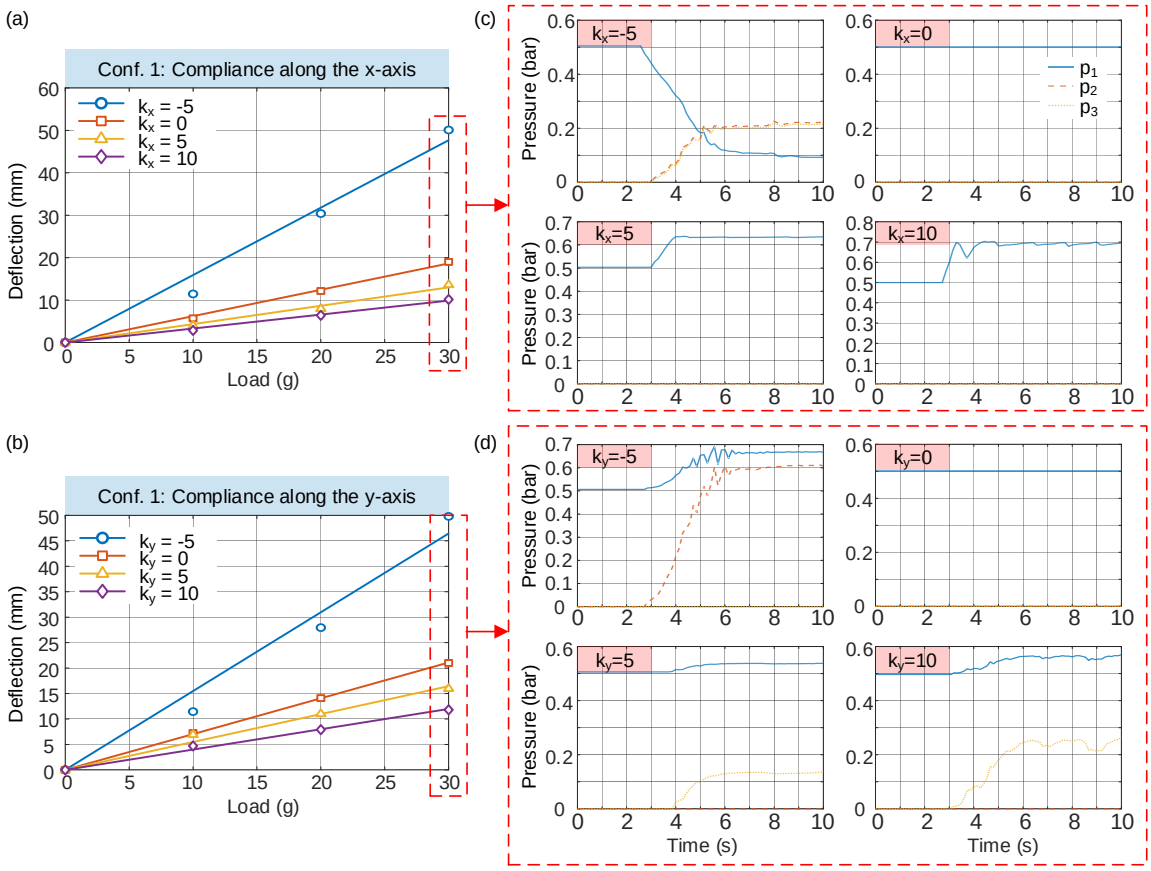

Fig. S3. Experimental results of directional stiffness validation under x- and y- direction loading. (a) Deflection–load relationships along the x-axis. (b) Deflection–load relationships along the x-axis. (c) Pressure responses of P_1, P_2, and P_3 under a 30 g lateral load for four k_x settings ($k_x = -5$, 0, 5, 10) mN/mm. (d) Pressure responses of P_1, P_2, and P_3 under a 30 g lateral load for four k_y settings ($k_y = -5$, 0, 5, 10) mN/mm.

Fig. S4(a) show the deflection–load curves along the x-axis in Configuration 2. The natural compliance along the x- direction at $k_x = 0$ mN/mm was $0.67\,\mathrm{mm\,g^{-1}}$. At $k_x = -5$ mN/mm, compliance increased to $1.29\,\mathrm{mm\,g^{-1}}$ (92.53 %, softening), whereas $k_x = 10$ mN/mm reduced it to $0.39\,\mathrm{mm\,g^{-1}}$ (−41.79 %, stiffening). Fig. 4(c) show the pressure responses during x-axis regulation. At $k_x = 0$ mN/mm, $P_2 \approx 0.5\,\mathrm{bar}$ and $P_1 = P_3 \approx 0\,\mathrm{bar}$. For $k_x = -5$ mN/mm, P_2 and P_3 both increase while P_1 remains near zero, resulting in softening. For $k_x = 5$ mN/mm and $k_x = 10$ mN/mm, P_2 decreases below baseline while P_1 increases to stiffening the robot.

Fig. S4 (b) show the deflection–load curves along the y- axis in Configuration 2. The natural compliance along the y-direction at $k_y = 0$ mN/mm was $0.60\,\mathrm{mm\,g^{-1}}$. At $k_y = -5$ mN/mm, compliance increased to $0.98\,\mathrm{mm\,g^{-1}}$ (63.33 %, softening), while $k_y = 10$ mN/mm reduced it to $0.31\,\mathrm{mm\,g^{-1}}$ (−48.33 %, stiffening). Fig. 4 (d) show the chamber pressures during y-axis regulation. At $k_y = 0$ mN/mm, $P_2 \approx 0.5\,\mathrm{bar}$ and $P_1 = P_3 \approx 0\,\mathrm{bar}$. For $k_y = -5$, P_2 increases significantly while $P_1, P_3 \approx 0$, enhancing softening. For $k_y = 5$ mN/mm and $k_y = 10$ mN/mm, P_2 decreases below baseline and P_1 increases, shifting force contribution to achieve stiffening.

Table II summarises compliance/stiffness variation ratios in both configurations. Across all cases, negative gains ($k_{x/y} < 0$) lead to increased compliance (softening), while positive gains ($k_{x/y} > 0$) reduce compliance (stiffening), and the tuning effect becomes more significant at larger gain values (e.g., $k = 10$ mN/mm shows much stronger stiffening than $k = 5$ mN/mm).

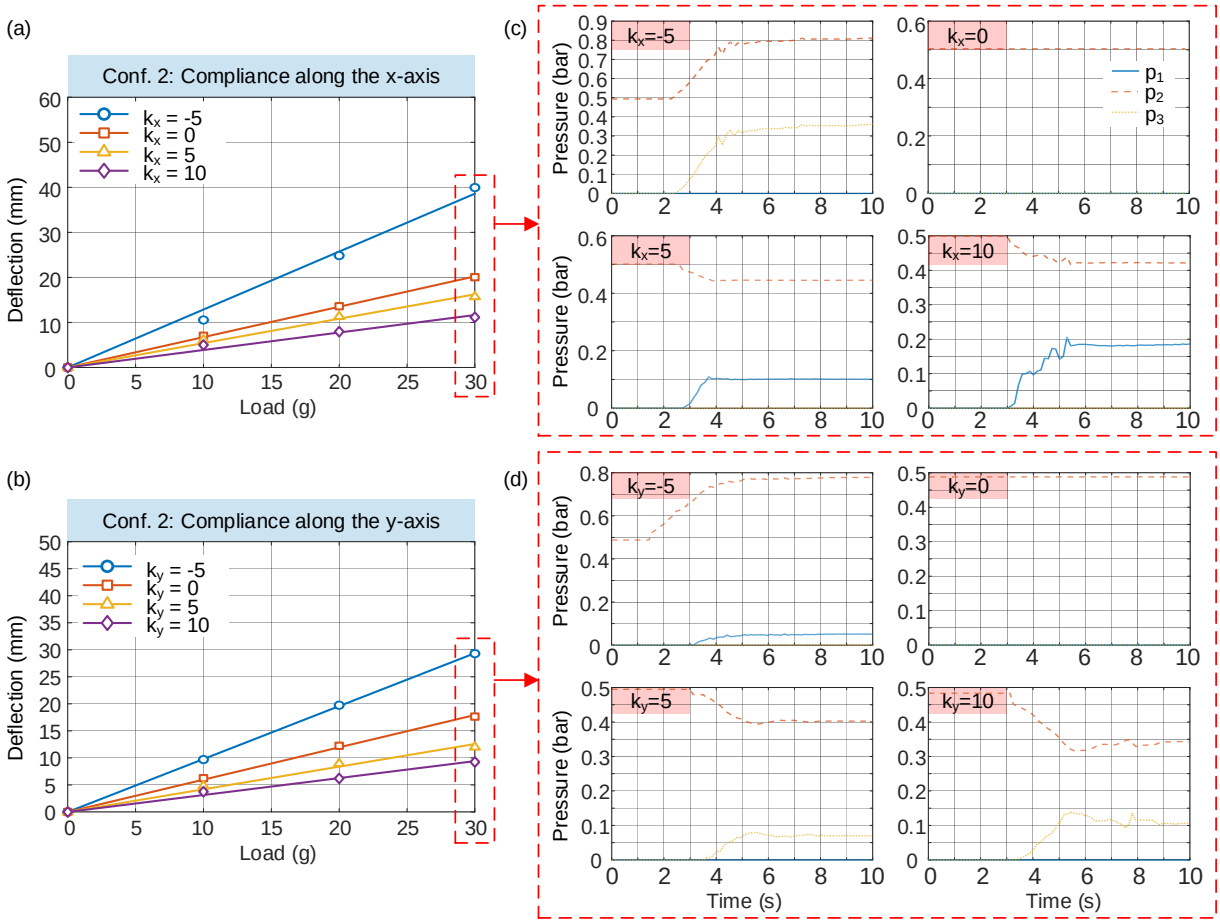

Fig. S4. Experimental results of directional stiffness validation under x- and y- direction loading (Configuration 2). (a) Deflection–load relationships along the x-axis. (b) Deflection–load relationships along the x-axis. (c) Pressure responses of P_1, P_2, and P_3 under a 30 g lateral load for four k_x settings ($k_x = -5$, 0, 5, 10) mN/mm. (d) Pressure responses of P_1, P_2, and P_3 under a 30 g lateral load for four k_y settings ($k_y = -5$, 0, 5, 10) mN/mm.

TABLE SII
COMPLIANCE ALONG THE x- AND y-AXES UNDER DIFFERENT GAIN FACTORS.

		Configuration 1		**Configuration 2**	
	Gain factor	**Compliance[mm/g] (Stiffness[g/mm])**	**Variation ratio**	**Compliance[mm/g] (Stiffness[g/mm])**	**Variation ratio**
Compliance/Stiffness along the x-axis	$k_x = -5$	1.59 (0.63)	+156.45% (-60.87%)	1.29 (0.78)	+92.53% (-47.65%)
	$k_x = 0$	0.62 (1.61)	0%	0.67 (1.49)	0%
	$k_x = 5$	0.43 (2.33)	−30.65% (+44.72%)	0.54 (1.85)	−19.40% (+24.16%)
	$k_x = 10$	0.33 (3.03)	−46.77% (+88.20%)	0.39 (2.56)	−41.79% (+71.81%)
Compliance/Stiffness along the y-axis	$k_y = -5$	1.55 (0.65)	+121.43% (-54.55%)	0.98 (1.02)	+63.33% (-38.92%)
	$k_y = 0$	0.70 (1.43)	0%	0.60 (1.67)	0%
	$k_y = 5$	0.55 (1.82)	−21.43% (+27.27%)	0.42 (2.38)	−30.00% (+42.51%)
	$k_y = 10$	0.40 (2.5)	−42.86% (+74.83%)	0.31 (3.23)	−48.33% (+93.41%)

C. Stability Analysis of the Compliance Control

The proposed approach falls within the framework of force-based impedance control [1], which is known for its robustness to model uncertainties and its ability to achieve stable contact interactions, even in stiff environments. However, as noted in [1], the realisation of high desired stiffness typically requires larger control gains and may amplify measurement noise, thereby increasing the risk of instability. Conversely, low stiffness settings can degrade position accuracy during free-motion phases. Accordingly, in this work, stability is defined as the ability of the system to avoid unstable oscillatory behaviour under stiffening control when subjected to external loads, while ensuring convergence to its initial equilibrium configuration once the external loads are removed.

When the gain factor is positive (stiffening mode) along the x- and y-axes, stability is preserved as the compliance decreases by approximately 40%–50%, corresponding to a stiffness increase of about 70%–95% (see Table SII) across both configurations. Conversely, when the gain factor is negative (softening mode), stability is maintained as the compliance increases

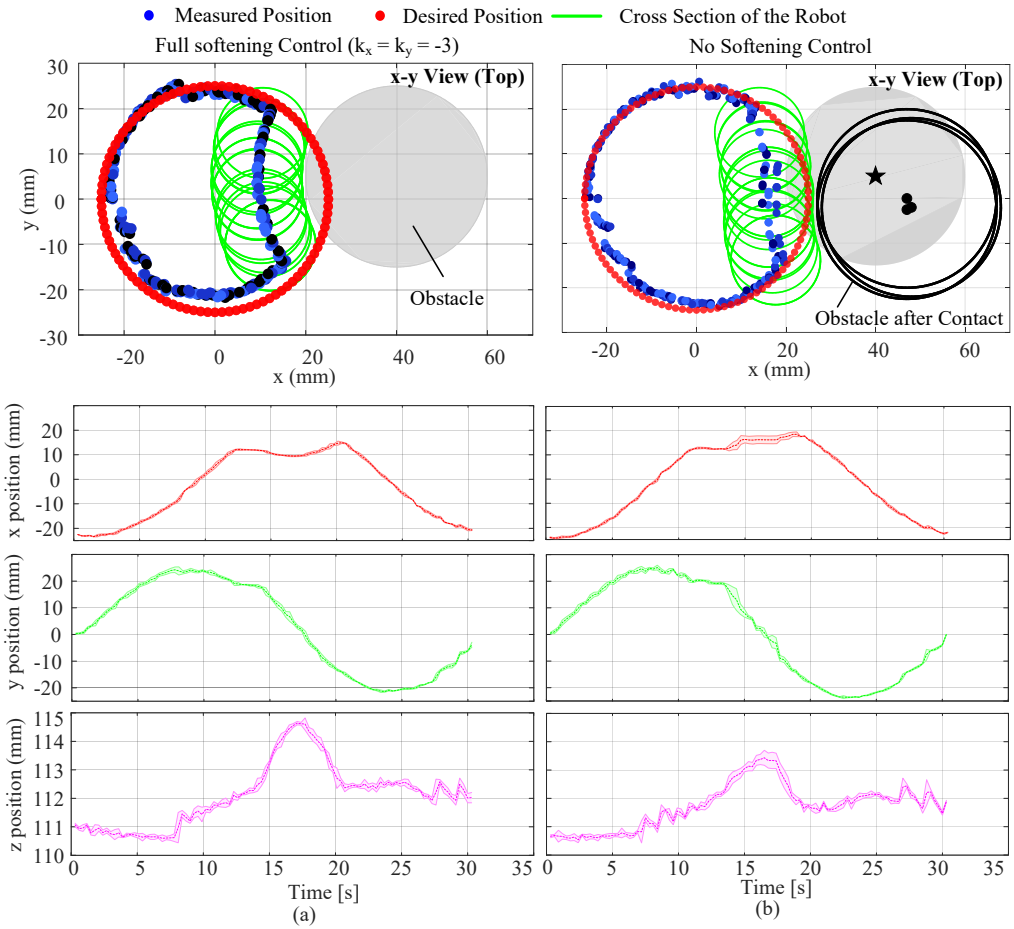

Fig. S5. Repeatability analysis under (a) full-softening control and (b) no softening control during 2D circular trajectory tracking with an obstacle. Each condition was evaluated over three trials. The shaded region represents the standard deviation, while the dashed line indicates the mean trajectory across the three trials.

by approximately 60%–150%, i.e., when the stiffness decreases by about 40%–60%. These results indicate that the proposed controller maintains stability for regulated stiffness factors within ± 1 relative to the nominal stiffness.

A similar trend is observed when regulating stiffness along the z-axis, albeit over a narrower range (see Table SI). Stability is maintained for stiffness increases of approximately 66%–100% relative to the nominal value. In contrast, under softening control, the stiffness can be reduced by approximately 20%–40% while preserving stable behavior.

It is noteworthy that a stiffness controller for a tendon-driven continuum robot was investigated in [2]. The results show that the controller can reduce the natural stiffness by approximately a factor of two in the y-direction, while increasing it by a similar factor in the x-direction, which is consistent with our findings. However, the approach in [2] was unable to modulate the stiffness along the z-direction, primarily due to friction compensation. In contrast, the proposed controller enables effective stiffness regulation along the z-axis.

D. Repeatability Analysis across Different Trials

Fig. S5 presents the results under full-softening control and no softening control during 2D circular trajectory tracking with an obstacle. Each control condition was evaluated over three trials. High tracking repeatability is observed in both cases, with the maximum width of the shaded region consistently remaining below 1 mm. In addition, without stiffening control, the averaged obstacle displacement across three trial is 10.3 mm, with a standard deviation of 1.2 mm.

REFERENCES

[1] C. Ott, R. Mukherjee, and Y. Nakamura, "A hybrid system framework for unified impedance and admittance control," vol. 78, no. 3, pp. 359–375, 2015.
[2] M. Mahvash and P. E. Dupont, "Stiffness control of surgical continuum manipulators," *IEEE Trans. Robot.*, vol. 27, no. 2, pp. 334–345, 2011.